Cascaded Pumping Cycle Control for Rigid Wing Airborne Wind Energy Systems

Rapp, Sebastian; Schmehl, Roland; Oland, Espen; Haas, Thomas

DOI
10.2514/1.G004246

Publication date
2019

Document Version
Final published version

Published in
Journal of Guidance, Control, and Dynamics: devoted to the technology of dynamics and control

Citation (APA)
Rapp, S., Schmehl, R., Oland, E., & Haas, T. (2019). Cascaded Pumping Cycle Control for Rigid Wing Airborne Wind Energy Systems. *Journal of Guidance, Control, and Dynamics: devoted to the technology of dynamics and control*, *42*(11), 2456-2473. https://doi.org/10.2514/1.G004246

Cascaded Pumping Cycle Control for Rigid Wing Airborne Wind Energy Systems

Sebastian Rapp* and Roland Schmehl†
Delft University of Technology, 2629 HS Delft, The Netherlands
Espen Oland‡
Kitemill AS, 5700 Voss, Norway
and
Thomas Haas§
KU Leuven, 3001 Leuven, Belgium

DOI: 10.2514/1.G004246

Airborne wind energy is an emerging technology that uses tethered unmanned aerial vehicles for harvesting wind energy at altitudes higher than conventional towered wind turbines. To make the technology competitive to other renewable energy technologies a reliable control system is required that allows autonomously operating the system throughout all phases of flight. In the present work a cascaded nonlinear control scheme for reliable pumping cycle control of a rigid wing airborne wind energy system is proposed. The high-level control strategy in the form of a state machine as well as the flight controller consisting of path-following guidance and control, attitude, and rate loop is presented along with a winch controller for tether force tracking. A mathematical model for an existing prototype will be derived, and results from a simulation study will be used to demonstrate the robustness of the proposed concept in the presence of turbulence and wind gusts.

I. Introduction

AIRBORNE wind energy (AWE) is an emerging branch within the sustainable energy systems portfolio that aims to exploit wind energy resources at altitudes higher than conventional towered wind turbines by means of kites and tethered aircraft. In general, AWE systems can be subdivided into two main categories. On the one hand, AWE systems with on-board generators can fly crosswind patterns with constant tether length. The kinetic energy of the relative flow is in this case directly converted into electrical power, and the electricity is transmitted via a conductive tether to the ground. On the other hand, AWE systems with a ground-based generator operate in a so-called *pumping cycle mode* and use the aerodynamic force of the kite or aircraft to uncoil the tether from a drum, which turns a generator that converts the mechanical torque into electrical power on the ground. When the maximum tether length is reached, the aircraft will fly back toward the ground station, while the tether is reeled in. Because the generator acts as a motor during this phase a fraction of the produced power is consumed. Once the minimum tether length is reached, the cycle starts all over again ([1] pp. 8–9, [2] pp. 2–4). A more detailed comparison of the different concepts can be found in [3]. In the present work the focus lies on the controller development for AWE systems operated in pumping cycle mode, although the controller can partially also be implemented for AWE systems that fly on a constant tether length.

Historically, most researchers in this field started to study the potential and controllability of AWE systems with flexible wings [4–8]. However, due to better scalability and efficiency the trend goes toward rigid wing AWE systems reflected by the fact that almost all companies in the field operate rigid wing prototypes. Nevertheless, available publications on rigid wing kite control are rare. Although the reliability of the control system plays a paramount role that decides upon the success of this new technology, most of the available literature focuses on flight path optimization instead of the development of more robust control solutions. One recent control approach that is not dedicated to flight path optimization is presented in [9]. In the paper, the authors focus on take-off and landing control, including a transition to a loiter-like figure-of-eight flight pattern on a constant tether length using linear controllers.

To the best of authors' knowledge, no modular control architecture for the full operational envelope for rigid wing AWE systems has been published yet. The term *modularity* is used to clearly distinguish the control approach from more integral approaches, usually based on nonlinear model predictive control such as in [10]. The present work tries to fill this gap where a modular control architecture similar to the one presented in [9], but eventually applicable to the whole range of operational modes, including take-off, transition, pumping cycle mode, and landing, is presented. Moreover, instead of using linear control techniques a model-based nonlinear flight controller is developed that eventually increases the operational envelope and the performance of the AWE system in situations where linear control techniques might fail. The modularity of the control architecture aims to achieve a high degree of reusability especially of the outer-loop module such that it can be implemented conveniently on different platforms. The modules have defined interfaces that allow to exchange, modify, and test different parts of the entire controller conveniently. This enables operators with existing prototypes to only use specific modules without the need to re-implement the entire control system. Especially the guidance module might be of interest for AWE companies, because it is entirely model independent, and can be implemented for AWE systems operated either in pumping cycle mode or on a fixed tether length with airborne generators. Furthermore, applying systematically the concept of pseudo control hedging [11] a flight envelope protection system is implemented, ensuring that no unfeasible commands are passed to the next loop. Constraining states is of particular importance in this application because the aircraft is usually operated at near-stall conditions while following a three-dimensional curved path that requires to constrain commands from the outer loops in a systematic manner. Such an envelope protection for AWE systems has not been presented yet

Presented as Paper 2019-1419 at the 2019 AIAA SciTech Forum, San Diego, CA, 7–11 January 2019; received 2 December 2018; revision received 29 April 2019; accepted for publication 6 May 2019; published online 30 May 2019.

*Ph.D. Researcher, Faculty of Aerospace Engineering, Kluyverweg 1; s.rapp@tudelft.nl. Member AIAA.

†Associate Professor, Faculty of Aerospace Engineering, Kluyverweg 1; r.schmehl@tudelft.nl.

‡Control System Manager, Miltzowsgate 2; eo@kitemill.no.

§Ph.D. Researcher, Department of Mechanical Engineering, Celestijnenlaan 300; thomas.haas@kuleuven.be.

apart from model predictive control approaches where constraints are directly embedded in the optimal control problem formulation [10].

The performance of the control system is demonstrated by means of a simulation study. To create a realistic simulation framework a detailed aerodynamic analysis using computational fluid dynamics (CFD) and *XFLR5* calculations of the 5 kW prototype of *Kitemill AS* have been carried out. The robustness of the control system toward wind gusts and atmospheric turbulence is assessed using three-dimensional transient wind field data generated by large-eddy simulations of a pressure-driven boundary layer.

The contributions of the present paper to the research community can be summarized as follows. First, an extension of the path-following controller that has been previously developed by one of the authors for flexible kite power systems is presented such that it can also be implemented for rigid wing AWE systems. Furthermore, we present an intuitive way to calculate the required tangential plane course rate according to the three-dimensional path curvature to keep the aircraft on the path. Moreover, an approach for radial direction control using tether force tracking is presented, and it will be demonstrated that this approach can be used at the same time for gust load alleviation. For a complete pumping cycle control we additionally propose a retraction phase controller that has not been presented for rigid wing AWE systems in the literature yet. Finally, we present a detailed description of the Kitemill 5 kW prototype, which can be used in the future as a reference model for other researchers in this field.

The paper is structured as follows. In Sec. II the simulation models for aircraft, tether, ground station, and the wind field are presented. In Sec. III a detailed derivation of the different controllers is presented. Simulation results are presented in Sec. IV, followed by conclusions in Sec. V.

II. Reference Frames and Simulation Models

A. Reference Frames

Figure 1 displays the wind frame W, where the x_W axis is pointing in downwind direction, the z_W axis is the local Earth surface normal vector, and the y_W forms a right-hand coordinate system together with x_W and z_W. The origin of the W frame is at the ground station. Note that this definition of the wind frame differs from the conventional definition found in the aerospace literature, where the wind frame is a local body-fixed frame ([12] p. 76). Furthermore, Fig. 2 displays the tangential plane frame τ, which will be used as a reference frame for the guidance loop. The z_τ axis is pointing toward the origin of the wind frame W, and the x_τ axis points toward the zenith position that is located above the ground station. Note that the τ-frame is defined equivalently to the North-East-Down frame (O) (see ([13] p. 12)) for a small Earth with radius one and center at the origin of the W frame. The position of the aircraft with respect to the W frame will be given either in Cartesian coordinates x_W, y_W, and z_W or in spherical coordinates using longitude λ and latitude ϕ as well as the Euclidean distance of the aircraft to the origin of W. The body-fixed frame B ([14] p. 57), the kinematic frame K ([14] p. 58), and the aerodynamic frame A ([14] p. 61) are defined according to aerospace convention.

B. Tethered Aircraft Model

The control strategy in this work will be tested within a simulation environment. The aircraft simulation model represents the 5 kW prototype that has been developed by *Kitemill AS*. Relevant aircraft parameters are summarized in Table 1 and a visualization of the aircraft is shown in Fig. 3. The actuators of the aircraft are modeled as second-order systems with natural frequency ω_0 and relative damping ζ, including limits on deflections and deflection rates. The numerical values are summarized in Table 2. The aircraft is modeled as a standard six-degree-of-freedom rigid body with an additional term in the translational equations of motion representing the tether force. No additional term in the rotational dynamics appears because it is assumed that the tether is attached to the center of gravity of the aircraft. A detailed derivation of the governing equations of motion can be found, for instance, in [12]. The translational dynamics in the body-fixed frame B are defined as

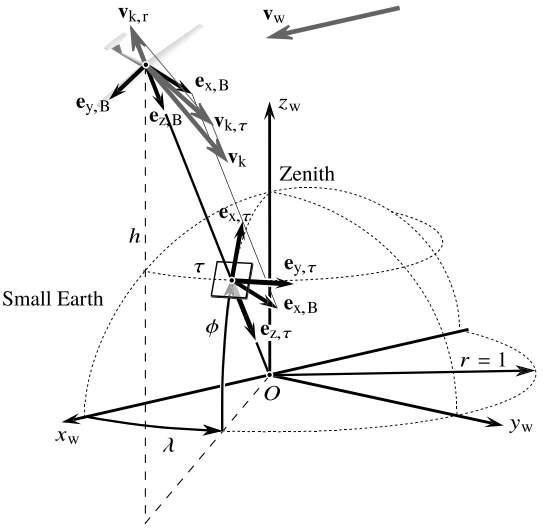

Fig. 1 Visualization of wind frame W, body-fixed frame B, and tangential plane frame τ.

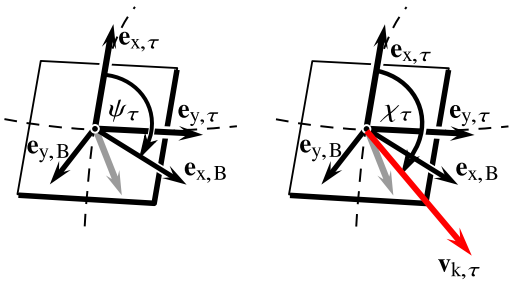

Fig. 2 Definition of the tangential plane heading Ψ_τ and tangential plane course χ_τ.

$$(\dot{\boldsymbol{v}}_k)_B = \begin{pmatrix} \dot{u}_k \\ \dot{v}_k \\ \dot{w}_k \end{pmatrix}_B = -(\boldsymbol{\omega}^{OB})_B \times (\boldsymbol{v}_k)_B + \frac{1}{m_k}((\boldsymbol{F}_a)_B + (\boldsymbol{F}_g)_B + (\boldsymbol{F}_t)_B) \tag{1}$$

where $(\boldsymbol{v}_k)_B \in \mathbb{R}^{3\times1}$ is the kinematic aircraft velocity in the B frame with components u_k, v_k, and w_k; m_k is the mass of the aircraft; $(\boldsymbol{\omega}^{OB})_B \in \mathbb{R}^{3\times1}$ is the angular velocity vector between the B and O frame containing the roll rate p, pitch rate q, and yaw rate r; $(\boldsymbol{F}_a)_B \in \mathbb{R}^{3\times1}$ is the aerodynamic force; $(\boldsymbol{F}_g)_B \in \mathbb{R}^{3\times1}$ is the gravity force; and $(\boldsymbol{F}_t)_B \in \mathbb{R}^{3\times1}$ is the tether force. All forces are defined with respect to the center of gravity. The aerodynamic force is modeled according to

$$(\boldsymbol{F}_a)_B = \frac{1}{2}\rho V_a^2 S_W \boldsymbol{M}_{BA} \begin{pmatrix} -C_D \\ C_Y \\ -C_L \end{pmatrix}_A \tag{2}$$

where $\rho = 1.225\ \mathrm{kg \cdot m^{-3}}$ is the air density and $\boldsymbol{M}_{BA}$ is the transformation matrix from the aerodynamic frame A to the body-

Table 1 Aircraft parameters

Parameter	Value	Unit
Aircraft mass m_k	4.778	kg
Inertia $J_{xx,yy,zz,xz}$	1.74, 0.28, 1.83, −0.02	$\mathrm{kg \cdot m^2}$
Wing area S_W	0.76	$\mathrm{m^2}$
Wingspan b	3.7	m
Mean chord $\bar{c}$	0.22	m

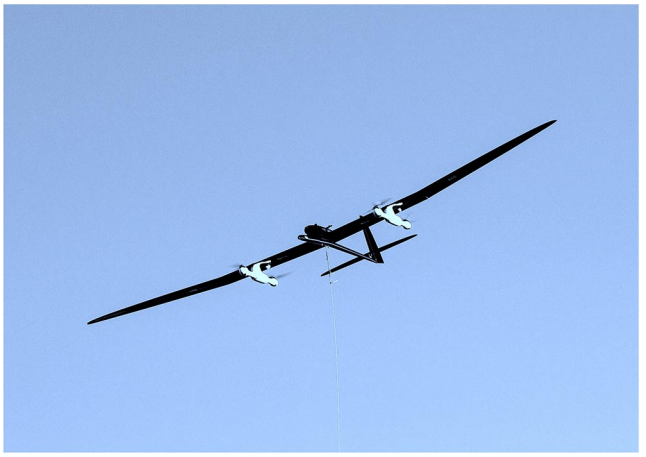

Fig. 3 Five-kilowatt prototype of Kitemill AS with vertical takeoff and landing capabilities.

fixed frame B ([12] p. 77). The coefficients C_D, C_Y, and C_L are nonlinear functions of the aircraft states and surface deflections. For the purpose of this paper, CFD and XFLR5 were used to create lookup tables that capture the main dependencies of the coefficients on states and surface deflections. The modeled dependencies on angle of attack, sideslip angle, and the control surface deflections are displayed in Figs. 4–6. Note that the contributions of the surface deflections to the drag coefficient were negligible and are therefore not displayed. Additionally, damping coefficients (see Table 3) are added, which in total yields

$$\begin{aligned} C_D &= C_D(\alpha) \\ C_Y &= C_Y(\beta, \delta_r) + C_{Y_p}\frac{pb}{2V_a} + C_{Y_r}\frac{rb}{2V_a} \\ C_L &= C_L(\alpha, \delta_e) + C_{L_q}\frac{q\bar{c}}{2V_a} \end{aligned} \tag{3}$$

where C_{Y_p}, C_{Y_r}, and C_{L_q} are defined in Table 3.

The rotational dynamics are defined as

$$(\dot{\omega}^{OB})_B = \begin{pmatrix} \dot{p} \\ \dot{q} \\ \dot{r} \end{pmatrix}_B = \boldsymbol{J}^{-1}(-(\boldsymbol{\omega}^{OB})_B \times \boldsymbol{J}(\boldsymbol{\omega}^{OB})_B + (\boldsymbol{M}_a)_B) \tag{4}$$

where $\boldsymbol{J} \in \mathbb{R}^{3x3}$ is the inertia tensor, and $(\boldsymbol{M}_a)_B \in \mathbb{R}^{3\times1}$ is the resulting aerodynamic moment around the center of gravity of the aircraft. Similar to the aerodynamic force, the aerodynamic moment is defined using moment coefficients:

$$(\boldsymbol{M}_a)_B = \frac{1}{2}\rho V_a^2 S_W \begin{pmatrix} bC_l \\ \bar{c}C_m \\ bC_n \end{pmatrix} \tag{5}$$

The relevant dependencies of the moment coefficients on states and surface deflections are depicted in Figs. 7–11. The damping terms are summarized in Table 4, which in total yields for the moment coefficients

Table 2 Actuator parameters

Parameter	Value	Unit
Natural frequency ω_0	35	rad/s
Relative damping ζ	1	—
Max./Min. aileron deflection	±15	°
Max./Min. elevator deflection	±15	°
Max./Min. rudder deflection	±20	°
Rate limits (all actuators)	±300	°/s

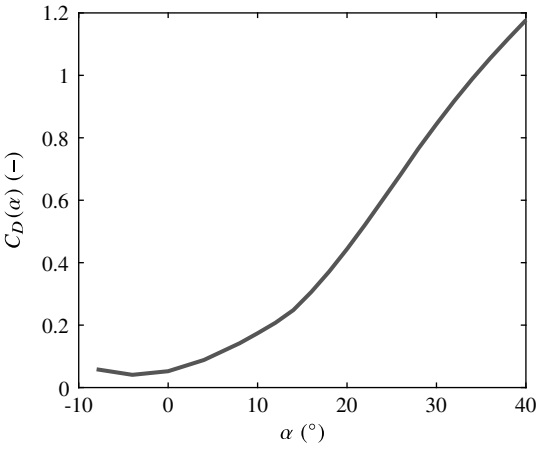

Fig. 4 Drag coefficient as a function of angle of attack.

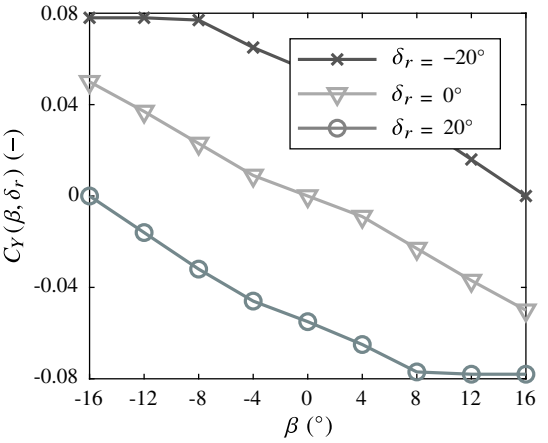

Fig. 5 Side force coefficient as a function of sideslip angle and rudder deflection.

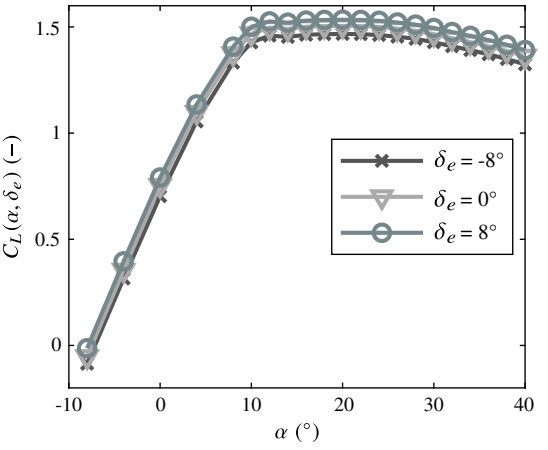

Fig. 6 Lift coefficient as a function of angle of attack and elevator deflection.

$$\begin{aligned} C_l &= C_l(\alpha, \delta_a) + C_l(\beta, \delta_r) + C_{l_p}\frac{pb}{2V_a} + C_{l_r}\frac{rb}{2V_a} \\ C_m &= C_m(\alpha, \delta_e) + C_{m_q}\frac{q\bar{c}}{2V_a} \\ C_n &= C_n(\alpha, \delta_a) + C_n(\beta, \delta_r) + C_{n_p}\frac{pb}{2V_a} + C_{n_r}\frac{rb}{2V_a} \end{aligned} \tag{6}$$

The attitude is parameterized using quaternions; hence the equation for the attitude propagation is given by

Table 3 Rate dependencies of the force coefficients

Coefficient	Value
C_{Yp}	−0.133
C_{Yr}	0.172
C_{Lq}	7.267

$$\dot{\boldsymbol{q}} = \begin{pmatrix} \dot{q}_1 \\ \dot{q}_2 \\ \dot{q}_3 \\ \dot{q}_4 \end{pmatrix} = \begin{pmatrix} -q_2 & -q_3 & -q_4 & q_1 \\ q_1 & -q_4 & q_3 & q_2 \\ q_4 & q_1 & -q_2 & q_3 \\ -q_3 & q_2 & q_1 & q_4 \end{pmatrix} \begin{pmatrix} p \\ q \\ r \\ 2k\kappa \end{pmatrix} \tag{7}$$

The quaternion attitude propagation equation [Eq. (7)] is implemented with gradient feedback as described in ([15] p. 64) with $\kappa = 1 - q_1^2 - q_2^2 - q_3^2 - q_4^2$; otherwise numerical inaccuracies can lead to a violation of the unity norm condition of the quaternion vector. The position of the aircraft's center of gravity $(\boldsymbol{p}^G)_O$ in the O frame will be propagated according to

$$(\dot{\boldsymbol{p}}^G)_O = \begin{pmatrix} \dot{p}_x^G \\ \dot{p}_y^G \\ \dot{p}_z^G \end{pmatrix}_O = \boldsymbol{M}_{OB} \begin{pmatrix} u_k \\ v_k \\ w_k \end{pmatrix}_B \tag{8}$$

where $\boldsymbol{M}_{OB}$ is the transformation matrix from the B to the O frame (see [12] p. 12).

The states of the tethered aircraft are the three kinematic velocity components in the body-fixed frame u_k, v_k, and w_k; the body rates p, q, and r; the quaternions q_1, q_2, q_3, and q_4; and the position in the O frame with components p_x^G, p_y^G, and p_z^G. At the moment full state feedback is assumed, and the controller requires measurements for mean wind direction on the ground ξ, position, velocity, orientation, angle of attack α, sideslip angle β, airspeed V_a, rotational rates, and the total tether force F_t measured on the ground and at the aircraft. The reason for measuring the tether force on the aircraft and on the ground is that due to the tether drag and weight the force measured on the ground differs from the tether force acting on the aircraft.

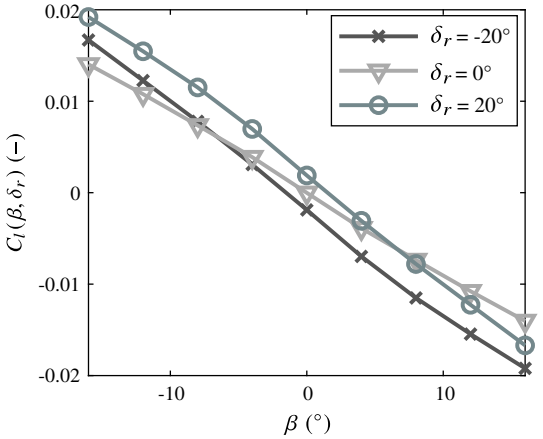

Fig. 7 Roll moment coefficient as a function of sideslip angle and rudder deflection.

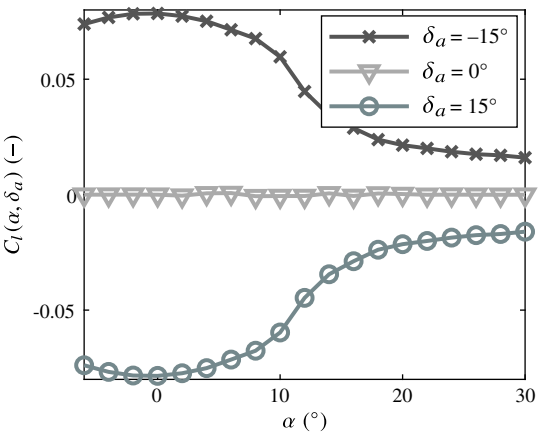

Fig. 8 Roll moment coefficient as a function of angle of attack and aileron deflection.

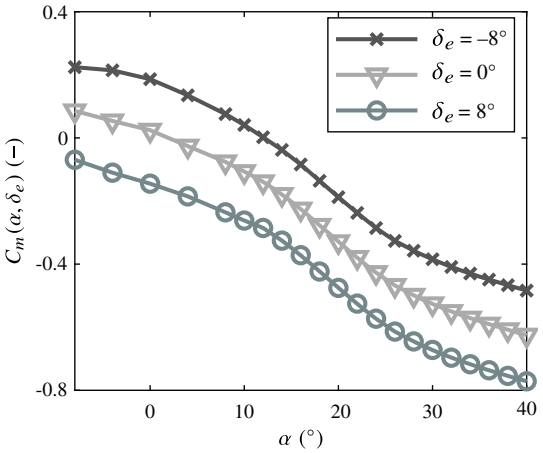

Fig. 9 Pitch moment coefficient as a function of angle of attack and elevator deflection.

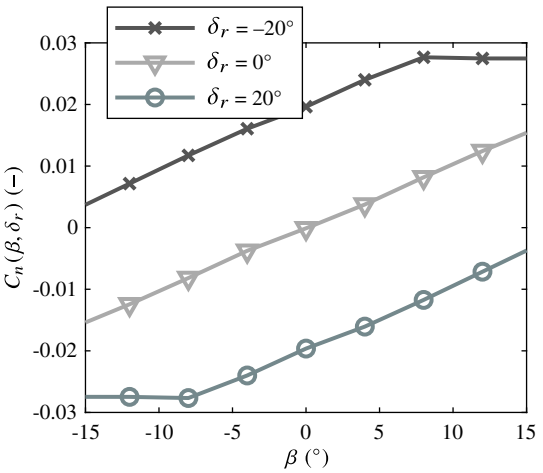

Fig. 10 Yaw moment coefficient as a function of sideslip angle and rudder deflection.

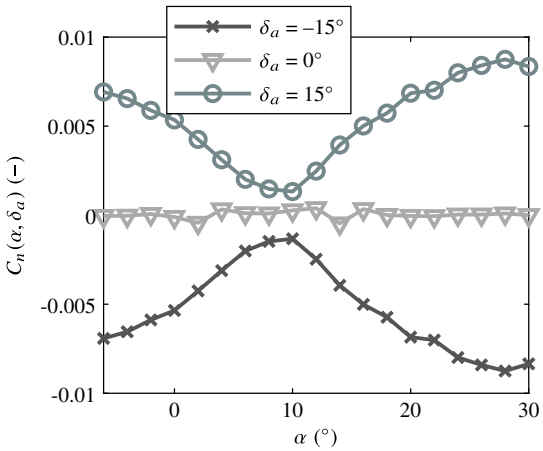

Fig. 11 Yaw moment coefficient as a function of angle of attack and aileron deflection.

Table 4 Damping coefficients

Coefficient	Value
C_{lp}	−0.6450
C_{lr}	0.2190
C_{mq}	−16.3740
C_{np}	−0.1310
C_{nr}	−0.0335

Table 5 Winch parameters

Parameter	Value	Unit
Winch radius r_W	0.1	m
Inertia J_W	0.08	$\mathrm{kg \cdot m^2}$
Viscous friction κ_W	0.6	$\mathrm{kg/(m \cdot s)}$

C. Tether Model

The tether is modeled as a particle system where the individual particles are connected via spring-damper elements. For each particle the point mass dynamics are formulated incorporating tether drag and tether weight. During reel-out or reel-in, the unstretched length of each spring-damper and the mass of each particle are adapted proportionally to the current change in tether length. A detailed explanation of the implemented tether model can be found in a previous work of the second author [16].

D. Ground Station

In general, the ground station consists of the generator and the winch. In this work the only relevant component for the controller development is represented by the winch, which can be modeled as a scalar first-order system given by

$$\dot{\omega}_w = J_w^{-1}(-\kappa_w \omega_w + r_w F_t + M_c) \tag{9}$$

where ω_W represents the rotational speed of the winch; r_W is the radius of the winch, which is assumed to be constant despite the reeling-in or reeling-out of the tether; $\kappa_W > \forall t$ is a viscous friction coefficient; F_t is the tether force; and M_c is the motor/generator torque, which represents the control input. The electrical drive system of the ground station is not modeled in this work. The used values for the winch are summarized in Table 5.

E. Wind Field Model

To test the controller in a realistic wind field, a four-dimensional velocity field is integrated into the simulation framework. The wind field data were generated by means of large-eddy simulations of a pressure-driven boundary layer. The computations were carried out using *SPWind*, a pseudo-spectral simulation code developed at KU Leuven. Information on the specification and the implementation of the flow solver can be found in [17–19]. The wind field data are available at a spatial resolution of approximately 20 m × 15 m × 7 m in x_W, y_W, and z_W directions, respectively, for a time series of several minutes and stored in the form of lookup tables. During the simulation the wind velocity vector at the location of the aircraft is obtained through linear interpolation of the adjacent vertex velocity vectors.

Table 6 State definitions

State	Description
π_0	Transition from take-off to aircraft mode
π_1	Capture crosswind pattern
π_2	Traction phase
π_3	Intermediate state
π_4	Transition to retraction
π_5	Retraction phase

III. Controller Development

A. Control Architecture and State Machine

The high-level control architecture is displayed in Fig. 12. On the highest level the controller can be decomposed into the flight and the winch control system, represented by the upper and lower cascades in Fig. 12. The task of the flight control system is to control the tangential motion on the sphere while the radial direction is controlled by the winch. The blocks correspond to modules that will be discussed in more detail in the following sections. In general, each block has one input and one output signal corresponding to the set point that has to be tracked by the module as well as the commanded set point for the next module. Blocks with two inputs are subdivided into two submodules (not displayed), one module for the traction and one for the retraction phase. All remaining modules are the same for both traction and retraction, although different gains and filter bandwidths are used for increased performance. Based on the current state π_i, as defined in Table 6, the output from either the traction or retraction module is passed on to the next module. The flight control guidance module input of the traction phase is the path parameterization $\mathbf{\Gamma}(s) \in \mathbb{R}^{3\times1}$ with $s \in (0, 2\pi)$. Within this module the required kinematic (subscript k) course $\chi_{k,c}$ and kinematic path angle $\gamma_{k,c}$ as well as the required course rate $\dot{\chi}_{k,c}$ and path angle rate $\dot{\gamma}_{k,c}$ are calculated based on the current position. The guidance module input of the retraction phase is the desired path angle $\bar{\gamma}_{k,c}$ and the output signal is the kinematic course $\chi_{k,c}$ and kinematic path angle $\gamma_{k,c}$. Note that $\bar{\gamma}_{k,c}$ and $\gamma_{k,c}$ differ from each other only in the final part of the retraction phase where the path angle $\bar{\gamma}_{k,c}$ is linearly increased to a fixed value before the transition back into the traction phase is triggered. This maneuver is used to dissipate kinetic energy of the aircraft before the turn. The path loop will track the commands from the guidance module and calculates attitude commands for aerodynamic (subscript a) bank angle $\mu_{a,c}$ and angle of attack α_c. Note that α and β always refer to the aerodynamic and not kinematic angles if not indicated otherwise. The attitude loop tracks the attitude

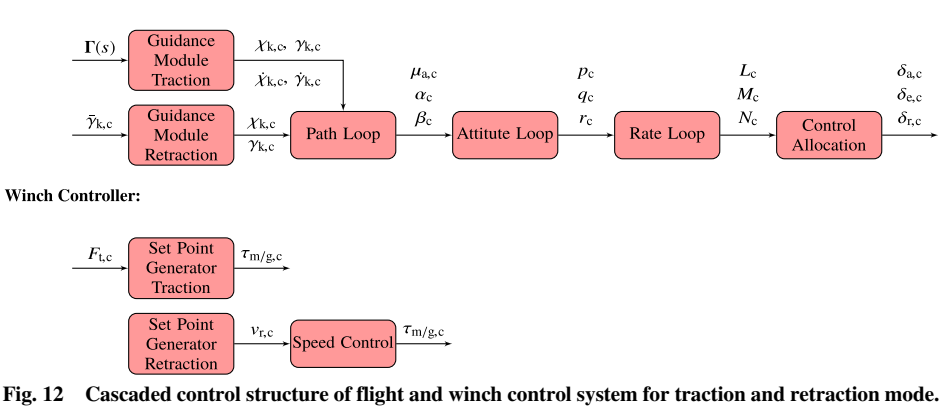

Fig. 12 Cascaded control structure of flight and winch control system for traction and retraction mode.

commands and transforms them into roll, pitch, and yaw rate commands p_c, q_c, and r_c, respectively. Finally, the rate loop calculates the control moments, which are then distributed among the actuators in the control allocation block, which results in an aileron command δ_a, elevator command δ_e, and rudder command δ_r. The winch controller requires only a set point generator for traction and retraction phase as well as a speed controller. During the traction phase, a reference torque $\tau_{m/g,c}$ is directly calculated based on the tether force set point $F_{t,c}$. During the retraction phase a fixed reeling in speed $v_{r,c}$ is commanded that will be tracked by a speed controller, which outputs a corresponding torque command $\tau_{m/g,c}$. In both cases, the torque commands will be tracked by the electrical drive control system.

Figure 13 shows the state-machine that is used to switch between the different control modules. The individual states are defined in Table 6. The modeled prototype of *Kitemill AS* allows vertical takeoff and landing (VTOL). A VTOL controller including the transition into pumping cycle mode is implemented in the simulation framework; however, a detailed description of the VTOL controller is out of the scope of this paper and will be part of a future publication. Essentially, a similar control approach for the winch and the flight controller is adapted from [20], where a VTOL controller for a flexible kite system is presented. The interface to the pumping cycle mode is given by a transition into π_0. In this work it will be assumed that the aircraft was guided in downwind direction to the operational altitude that fulfills the latitude condition $\phi > \phi_0 + \Delta_{\phi_0}$, where the VTOL controller keeps the aircraft in a hover state (not displayed) until π_0 is triggered. ϕ_0 is the mean latitude angle of the path and $0° \leq \Delta_{\phi_0} \leq 10°$ is a small offset. The transition from the launching state to the crosswind flight state is initiated by fast reeling in of the tether. As soon as the airspeed exceeds the minimum airspeed, here denoted with $V_{a,\min}$, the transition to π_1 is triggered. In this state the path-following controller is activated and the guidance law is initialized with a first guess of the closest point on the path relative to the current aircraft position. Flying toward the path decreases the elevation angle, which triggers the transition into the traction phase state π_2 if it reaches a value below $\phi_m + \Delta_t$ ($0° \leq \Delta_t \leq 10°$) and the winch starts reeling out the tether. The intermediate state π_1 was added to start reeling out after the aircraft is sufficiently steered into the downwind direction. If the tether is reeled out immediately this could lead to a drop in tether tension during the initial turn. As long as no landing is issued by the supervisory layer ($fVTOL = 1$) the kite remains in state π_2. The transition into π_3 is triggered as soon as the specified tether length is reached. This state can be interpreted as an intermediate state, which is left as soon as the aircraft flies into the negative half plane of the wind window defined by a negative longitude $\lambda < 0$. This triggers the transition to π_4. The retraction phase is initiated as soon as the aircraft flies past wp_1, which is defined as the outermost point on the path. This procedure ensures that before the reeling-in of the tether is triggered the aircraft always has to fly first downward through the center and hence flies toward the ground station always on the same side of the wind window. Before the aircraft transitions back into the traction mode, one out of three conditions has to be satisfied: Either the tether length or the Euclidean distance $\|\boldsymbol{p}^G\|$ of the aircraft relatively to the ground station is below a specified value, or the elevation angle of the aircraft exceeds a maximum value. The latter can be regarded as a safety mechanism that prevents the aircraft from overshooting the ground station.

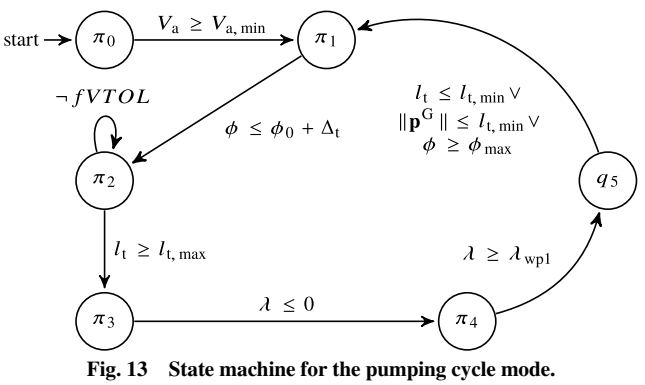

Fig. 13 State machine for the pumping cycle mode.

B. Guidance Modules

1. Traction Phase Guidance

In the existing AWE literature [6,7,21,22] the kite is steered according to the tangential plane course set point $\chi_{\tau,c}$. It is defined as the angle between the $\boldsymbol{e}_{x,\tau}$ axis of the tangential plane frame τ and the x axis of the kinematic frame K as depicted in Fig. 2. This strategy is mainly motivated by the fact that a direct relationship between the steering input of a flexible kite and the tangential plane course rate can be derived [8,23], which allows to directly calculate the steering input based on the course rate. In this work the guidance problem will be solved as well by first calculating the desired χ_τ course set point, which will be then, however, transformed into a corresponding set point for the course χ_k and path angle γ_k, which specify the orientation of the K frame relatively to the O frame. This approach provides an additional control degree of freedom to track the desired flight direction. Moreover, controlling course and path angle in the traction phase allows to use the same medium loop control structure for the retraction phase in which the kite is not steered on a tangential plane anymore. Furthermore, providing set points for course and path angle allows to integrate the guidance module easier into existing autopilot architectures for conventional aircraft. Hence this approach also fits better into the modular control philosophy proposed in this work.

Separating the radial and the tangential motion of the aircraft the control objectives for the traction phase can be stated as follows: On the one hand, the radial direction needs to be controlled by the winch such that the tether force set point is tracked. Moreover, the radial direction controller needs to ensure that the maximum tether tension is not exceeded to avoid tether rupture or aircraft damage. On the other hand, for the tangential motion control the aircraft position will be projected onto the unit sphere. In that case, the flight controller needs to follow a predefined flight path on a sphere with a constant radius of one. The path on the unit sphere is adapted proportionally to the distance of the aircraft to the ground station such that the real path the aircraft traces has a constant shape during the reel-out phase. Figure 14 depicts an example flight path, including a visualization of the aircraft and the flexible tether. Note that the depicted vectors and the aircraft model are scaled, and the physical flight path and not the path on the unit sphere that is used for the guidance is shown for visualization purposes.

Parts of the guidance module are based on a previous work of the second author [8] where it is used to steer a flexible kite along a prescribed path. In this work some modifications are introduced such as a novel predictive part that takes the instantaneous path curvature into account in order to calculate the reference course rate. Furthermore, the interface to a rigid wing aircraft path-following controller will be presented taking into account a generalization of the rotational rate vector $(\boldsymbol{\omega}^{\tau K})_{\bar{K}}$, which describes the relative rotation between the rotated kinematic and the tangential plane frame.

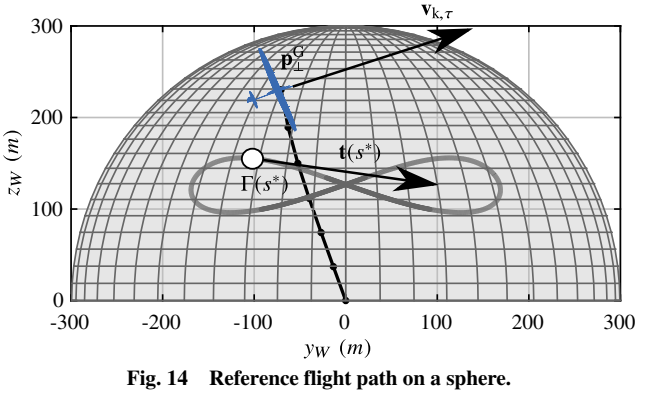

Fig. 14 Reference flight path on a sphere.

Because the terminology slightly deviates from [8], the main steps of the derivation will be presented again in addition to the novel extensions for completeness.

The objective of the guidance module is twofold. First, it needs to calculate the flight direction that leads to a reduction of the distance δ (i.e., the cross track error) as defined by the arc length between the projected aircraft position on the unit sphere $\boldsymbol{p}_{\perp}^{G}$ and the path $\boldsymbol{\Gamma}$. Second, for zero cross-track error the kinematic velocity vector projected onto the tangential plane $\boldsymbol{v}_{k,\tau}$ needs to be aligned with the path direction as defined by the tangent vector $\boldsymbol{t}$. For clarification, all relevant vectors are depicted in Fig. 14. The path is defined in spherical coordinates on the unit sphere; hence a point on the path is fully defined by its longitude λ_{Γ} and latitude ϕ_{Γ}. Note that all vectors are given in the W reference frame, if not indicated otherwise. In Cartesian coordinates the path is given as

$$\boldsymbol{\Gamma}(s) = \begin{pmatrix} \cos\lambda_{\Gamma}(s)\cos\phi_{\Gamma}(s) \\ \sin\lambda_{\Gamma}(s)\cos\phi_{\Gamma}(s) \\ \sin\phi_{\Gamma}(s) \end{pmatrix} \tag{10}$$

For subsequent calculations the tangent and its derivative need to be known. The tangent can be calculated according to

$$\boldsymbol{t}(s) = \frac{d\boldsymbol{\Gamma}}{ds} = \frac{\partial\boldsymbol{\Gamma}}{\partial\lambda_{\Gamma}}\frac{d\lambda_{\Gamma}}{ds} + \frac{\partial\boldsymbol{\Gamma}}{\partial\phi_{\Gamma}}\frac{d\phi_{\Gamma}}{ds} \tag{11}$$

and its derivative is given by

$$\boldsymbol{t}'(s) = \frac{\partial^2\boldsymbol{\Gamma}}{\partial\lambda_{\Gamma}^2}\left(\frac{d\lambda_{\Gamma}}{ds}\right)^2 + 2\frac{\partial^2\boldsymbol{\Gamma}}{\partial\phi_{\Gamma}\partial\lambda_{\Gamma}}\frac{d\phi_{\Gamma}}{ds}\frac{d\lambda_{\Gamma}}{ds} + \frac{\partial^2\boldsymbol{\Gamma}}{\partial\phi_{\Gamma}^2}\left(\frac{d\phi_{\Gamma}}{ds}\right)^2 + \frac{\partial\boldsymbol{t}}{\partial s} \tag{12}$$

The last partial derivative is given by

$$\frac{\partial\boldsymbol{t}}{\partial s} = \frac{\partial\boldsymbol{\Gamma}}{\partial\lambda_{\Gamma}}\frac{d^2\lambda_{\Gamma}}{ds^2} + \frac{\partial\boldsymbol{\Gamma}}{\partial\phi_{\Gamma}}\frac{d^2\phi_{\Gamma}}{ds^2} \tag{13}$$

Furthermore, the speed of the path parameter s is denoted with $ds/dt = \dot{s}$ and is given by the projection of the velocity vector onto the path tangent:

$$\frac{ds}{dt} = \dot{s} = \frac{\boldsymbol{t}^T(\boldsymbol{v}_k^G)_W}{\|\boldsymbol{t}\|_2\|(\boldsymbol{p}^G)_W\|_2} \tag{14}$$

The flight path can be fully described as a planar curve using scalar functions of s for longitude and latitude. The flight path in this work will be defined as a *Lemniscate of Booth*, given by

$$\begin{aligned} \lambda_{\Gamma}(s) &= \frac{a_{\text{Booth}}\sin s}{1 + (a_{\text{Booth}}/b_{\text{Booth}})^2\cos^2 s} \\ \phi_{\Gamma}(s) &= \frac{(a_{\text{Booth}}^2/b_{\text{Booth}})\sin s\cos s}{1 + (a_{\text{Booth}}/b_{\text{Booth}})^2\cos^2 s} \end{aligned} \tag{15}$$

which can be derived from the equation of a hyperbolic lemniscate as defined, for instance, in ([24] p. 164) with $y = x(a/b)\cos s$. a_{Booth} and b_{Booth} are parameters that define height and width of the curve. A detailed comparison with other curve parameterizations is out of the scope of this paper. Note, however, that the Lemniscate of Booth offers for a large range of width and height parameters smaller curvature peaks compared with the *Lissajous* figure parameterization used in [8], which is why it is chosen in this work. Ultimately, the planar curve can be transformed into a three-dimensional curve using Eq. (10).

The distance between a point on the curve and the kite position can be calculated using the definition of the arc length on the unit sphere.

$$\delta(s) = \arccos(\boldsymbol{p}_{\perp}^{G} \cdot \boldsymbol{\Gamma}(s)) \tag{16}$$

To determine the closest point (defined by s^*) requires to solve

$$\left.\frac{d\delta}{ds}\right|_{s=s^*} = 0 \tag{17}$$

where the derivative is given by

$$\frac{d\delta}{ds} = -\frac{1}{\sin\delta}\frac{d(\boldsymbol{p}_{\perp}^{G} \cdot \boldsymbol{\Gamma}(s))}{ds} = -\frac{\boldsymbol{p}_{\perp}^{G} \cdot \boldsymbol{t}(s)}{\sin\delta} \tag{18}$$

Eventually, the following root-finding problem needs to be solved:

$$\boldsymbol{p}_{\perp}^{G} \cdot \boldsymbol{t}(s) = 0 \tag{19}$$

The solution can be determined using, for instance, *Newton*'s method. With

$$\left(\frac{d}{ds}\right)\boldsymbol{p}_{\perp}^{G} \cdot \boldsymbol{t}(s) = \boldsymbol{p}_{\perp}^{G} \cdot \frac{d\boldsymbol{t}(s)}{ds} \tag{20}$$

The update equation for *Newton*'s method is then

$$s^{+} = s^{-} - \frac{\boldsymbol{p}_{\perp}^{G} \cdot \boldsymbol{t}(s)}{\boldsymbol{p}_{\perp}^{G} \cdot \boldsymbol{t}'(s)} \tag{21}$$

In the simulations, the method converged usually quickly after two to three iterations if the previous solution is selected as a starting point.

Knowing the closest point on the curve relative to the current aircraft position enables to calculate the desired flight direction. The vector at the current aircraft position pointing toward $\boldsymbol{\Gamma}(s^*)$ perpendicularly along a great circle can be expressed as

$$\boldsymbol{b}^{G} = \frac{\boldsymbol{\Gamma}(s^*) - \cos\delta\boldsymbol{p}_{\perp}^{G}}{\sin\delta} \tag{22}$$

This can be derived simply by looking at the normal projection of $\boldsymbol{\Gamma}(s^*)$ onto $\boldsymbol{p}_{\perp}^{G}$ (see Fig. 15) given by

$$\boldsymbol{\Gamma}_{\text{proj}}(s^*) = \cos\delta\boldsymbol{p}_{\perp}^{G} \tag{23}$$

and

$$\boldsymbol{\Gamma}_{\perp}(s^*) = \boldsymbol{\Gamma}(s^*) - \boldsymbol{\Gamma}_{\text{proj}}(s^*) \tag{24}$$

where $-\boldsymbol{\Gamma}_{\perp}(s^*)$ denotes the vector of the projection direction, which is by definition perpendicular to $\boldsymbol{p}_{\perp}^{G}$. Normalizing $\boldsymbol{\Gamma}_{\perp}(s^*)$ yields:

$$\boldsymbol{b}^{G} = \frac{\boldsymbol{\Gamma}(s^*) - \boldsymbol{\Gamma}_{\text{proj}}(s^*)}{\|\Gamma(s^*) - \boldsymbol{\Gamma}_{\text{proj}}(s^*)\|_2} = \frac{\boldsymbol{\Gamma}(s^*) - \cos\delta\boldsymbol{p}_{\perp}^{G}}{\sin\delta} \tag{25}$$

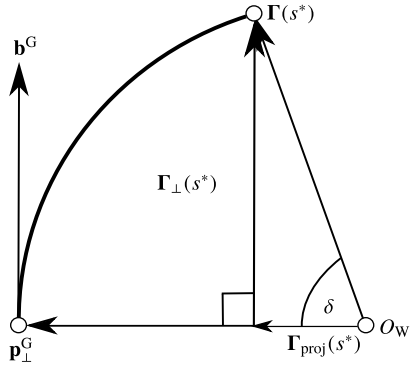

Fig. 15 A slice of the unit sphere containing a segment of the great circle that connects $\boldsymbol{p}_{\perp}^{G}$ with $\boldsymbol{\Gamma}(s^*)$.

Equation (19) can be rewritten using Eq. (25):

$$\frac{\boldsymbol{\Gamma}(s^*)\cdot\boldsymbol{t}(s^*)-\sin\delta(\boldsymbol{b}^G\cdot\boldsymbol{t}(s^*))}{\cos\delta}=0 \tag{26}$$

The first scalar product is zero, since $\boldsymbol{\Gamma}(s^*)$ is perpendicular to the tangent vector, which yields

$$\tan\delta(\boldsymbol{b}^G\cdot\boldsymbol{t}(s^*))=0 \tag{27}$$

If this equation is divided by $\tan\delta$ (bearing in mind that the only relevant singularity is located at $\delta=0$), this yields for $\delta\neq 0$

$$\boldsymbol{b}^G\cdot\boldsymbol{t}(s^*)=0 \tag{28}$$

which proves that the direction vector pointing toward the path is indeed orthogonal to the tangent at $\boldsymbol{\Gamma}(s^*)$. Hence, if the kite would fly in $\boldsymbol{b}^G$ direction it would intercept the path perpendicularly. From a practical point of view it is, however, not desired that the aircraft intercepts the path perpendicularly. Instead, it is desirable that the commanded flight direction smoothly transitions from an orthogonal interception if the aircraft is farther away from the curve to a tangential, hence curve aligned, flight direction. If the aircraft is on the path it is desired that the path controller tracks the directional angle of the tangent vector on the curve. This behavior can be achieved as follows: If $\delta\neq 0$, the course angle $\chi_{\tau,\parallel}$, which can be obtained from the tangent on the path, has to be adapted such that the distance to the curve δ decreases over time. In [8] the following set point definition is proposed, which is used in this work as well:

$$\chi_{\tau,c}=\chi_{\tau,\parallel}+\Delta\chi_\tau \tag{29}$$

with

$$\Delta\chi_\tau=\arctan_2(-\sigma(\iota)\delta,\delta_0) \tag{30}$$

and

$$\iota=(\boldsymbol{t}(s^*)\times\boldsymbol{\Gamma}(s^*))\cdot(\boldsymbol{p}_\perp^G-\Gamma(s^*)) \tag{31}$$

where σ denotes the sign of ι. Depending on if the aircraft is on the left- or right-hand side of the path, as depicted in Fig. 16, the sign of $\Delta\chi_\tau$ is adapted accordingly. If the course as defined in Eq. (29) is tracked by the flight control system, the relative distance δ between aircraft and path decreases over time; that is, $\dot\delta<0$, which can be proven as follows. Taking the derivative of Eq. (16) with respect to time at $s=s^*$ yields

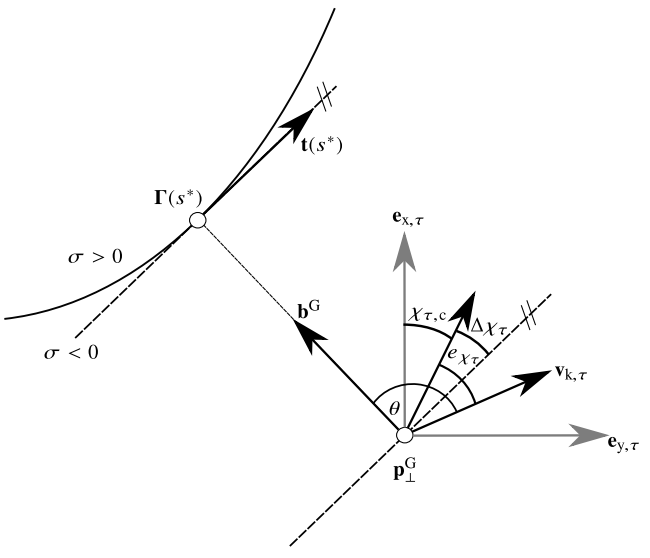

Fig. 16 Visualization of the angles used in Eq. (38).

$$\dot\delta=-\frac{1}{\sqrt{1-\cos^2\delta}}(\dot{\boldsymbol{p}}_\perp^G\cdot\boldsymbol{\Gamma}(s^*)+\boldsymbol{p}_\perp^G\cdot\dot{\boldsymbol{\Gamma}}(s^*)) \tag{32}$$

with

$$\dot{\boldsymbol{\Gamma}}(s^*)=\boldsymbol{t}(s^*)\dot s^* \tag{33}$$

$\boldsymbol{p}_\perp^G\cdot\boldsymbol{t}(s^*)$ is zero; therefore,

$$\dot\delta=-\frac{1}{\sin\delta}(\dot{\boldsymbol{p}}_\perp^G\cdot\boldsymbol{\Gamma}(s^*)) \tag{34}$$

With Eq. (25) the dot product can be written as

$$\dot{\boldsymbol{p}}_\perp^G\cdot\boldsymbol{\Gamma}(s^*)=\dot{\boldsymbol{p}}_\perp^G\cdot\boldsymbol{b}^G\sin\delta+\dot{\boldsymbol{p}}_\perp^G\cdot\boldsymbol{p}_\perp^G\cos\delta \tag{35}$$

Per definition, the second scalar product on the right-hand side is zero. Inserting the result into Eq. (34) yields

$$\dot\delta=-\dot{\boldsymbol{p}}_\perp^G\cdot\boldsymbol{b}^G \tag{36}$$

This can be further simplified to

$$\dot\delta=-v_{k,\tau}\cos\theta \tag{37}$$

where $v_{k,\tau}$ is the magnitude of $\boldsymbol{v}_{k,\tau}=\dot{\boldsymbol{p}}_\perp^G$ and θ denotes the angle between the vector pointing perpendicularly to $\Gamma(s^*)$ and the projected aircraft velocity on the tangential plane. To calculate θ two cases have to be distinguished:

$$\theta=\begin{cases}\pi/2-\Delta\chi_\tau+e_{\chi_\tau}, & \text{for } \sigma<0\\ \pi/2+\Delta\chi_\tau-e_{\chi_\tau}, & \text{for } \sigma>0\end{cases} \tag{38}$$

This yields for $\dot\delta$

$$\dot\delta=\begin{cases}-v_{k,\tau}\sin(\Delta\chi_\tau-e_{\chi_\tau}), & \text{for } \sigma<0\\ -v_{k,\tau}\sin(-\Delta\chi_\tau+e_{\chi_\tau}), & \text{for } \sigma>0\end{cases} \tag{39}$$

with Eq. (30) it follows

$$\begin{aligned}\dot\delta&=-\sigma v_{k,\tau}\sin(-\Delta\chi_\tau+e_{\chi_\tau})\\&=-\sigma v_{k,\tau}(-\sin\Delta\chi_\tau\cos e_{\chi_\tau}+\cos\Delta\chi_\tau\sin e_{\chi_\tau})\\&=-\sigma v_{k,\tau}\left(\frac{\sigma\delta/\delta_0\cos e_{\chi_\tau}}{\sqrt{1+(\delta/\delta_0)^2}}+\frac{\sin e_{\chi_\tau}}{\sqrt{1+(\delta/\delta_0)^2}}\right)\\&=\frac{-\sigma v_{k,\tau}}{\sqrt{1+(\delta/\delta_0)^2}}(\sigma\delta/\delta_0\cos e_{\chi_\tau}+\sin e_{\chi_\tau})\end{aligned} \tag{40}$$

where the identities

$$\begin{aligned}\sin(\arctan(x))&=x/\sqrt{1+x^2}\qquad \cos(\arctan(x))=1/\sqrt{1+x^2}\\ \sin(x+y)&=\sin(x)\cos(y)+\cos(x)\sin(y)\end{aligned} \tag{41}$$

have been used. If the course error dynamics are asymptotically stable, that is, $e_{\chi_\tau}\to 0$, then

$$\dot\delta=-v_{k,\tau}\frac{\delta/\delta_0}{\sqrt{1+(\delta/\delta_0)^2}} \tag{42}$$

where the fact that $\sigma^2=1$ has been exploited. Equation (42) shows that if the commanded course according to Eq. (29) is tracked, the distance δ strictly decreases over time, which concludes the proof.

The input signal to the path-following controller will be the desired course and flight path angle rates. In an inversion-based control approach these rates are usually obtained by filtering the corresponding course and flight path angles. From a geometrical

point of view, the reference course rate contains information about the future course angle and hence is linked to the curvature of the path that needs to be followed. If the rate of a reference filter is used, only an approximation is obtained if the to-be-followed path is not a straight line, or a combination thereof, which results in step commands in the course reference angle that only require a course rate in the transients. If the path curvature is not zero the approximated rate by the filter will not keep the system on the path because in general the rate of the filter does not correspond to the rate imposed by the geometry of the path. Hence, although the path-following controller would steer the aircraft toward the path, once the aircraft is on the path it would leave the path again, which can lead to unnecessary control effort and oscillations of the aircraft around the path. Theoretically, this effect can be minimized with high gain tracking error feedback, which, however, can lead to an unstable closed-loop system. To avoid this behavior a different approach is pursued where the exact required course rate based on the path geometry will be calculated analytically instead of numerically using a filter. The commanded tangential plane course rate is given by $\chi_{\tau,c}$, and hence the commanded rate can be calculated by taking the derivative of the terms in Eq. (29), which yields

$$\dot{\chi}_{\tau,c} = \dot{\chi}_{\tau,\parallel} + \dot{\Delta}\chi_\tau \tag{43}$$

with

$$\dot{\Delta}\chi_\tau = -\frac{\sigma/\delta_0}{1+(\delta/\delta_0)^2}\dot{\delta} \tag{44}$$

with Eq. (42) this leads to

$$\dot{\Delta}\chi_\tau = \frac{v_{k,\tau}\sigma/\delta_0^2}{(1+(\delta/\delta_0)^2)^{3/2}}\delta \tag{45}$$

It can be seen that for decreasing δ, hence small δ/δ_0, the contribution of $\dot{\Delta}\chi_\tau$ converges linearly to zero. Note that $\dot{\Delta}\chi_\tau$ is not linked to the path geometry directly. It improves, however, the path-following performance if $\delta \neq 0$. If $\dot{\Delta}\chi_\tau$ would be neglected, only the course error feedback part would adapt $\dot{\chi}_{\tau,\parallel}$ such that the commanded course rate does not only contain a component that would keep the aircraft parallel to the path. Because this contribution is mainly required for $\delta \neq 0$, a too high gain for the course tracking feedback would probably dominate also $\dot{\chi}_{\tau,\parallel}$ for $\delta = 0$. Hence, using a small gain for the course error feedback in combination with the additional feed-forward part $\dot{\Delta}\chi_\tau$ increases the performance of the path-following controller. The derivative of $\chi_{\tau,\parallel}$ is given by

$$\dot{\chi}_{\tau,\parallel} = \frac{d}{dt}\arctan\left(\frac{\boldsymbol{e}_{y,\tau}\cdot\boldsymbol{t}^G}{\boldsymbol{e}_{x,\tau}\cdot\boldsymbol{t}^G}\right) \tag{46}$$

where u_k^G and v_k^G are the x and y components of the kinematic velocity vector of the aircraft in the τ reference frame. Equation (47) defines the rate with which the angle between the tangent vector $\boldsymbol{t}^G$ at the aircraft and the basis vector of the tangent plane frame $\boldsymbol{e}_{x,\tau}$ changes as a function of path geometry and aircraft velocity. It hence corresponds to the required course rate imposed by the path curvature.

Using kinematic manipulations the desired tangential plane course rate $\dot{\chi}_{\tau,c}$ can be converted into the corresponding rates for the course and flight path angle $\dot{\chi}_{k,c}$ and $\dot{\gamma}_{k,c}$, respectively. The tangential plane course rate occurs in the angular velocity vector between the τ and the $\bar{K}$ frame, for instance, given in the rotated kinematic frame $\bar{K}$:

$$(\boldsymbol{\omega}^{\tau\bar{K}})_{\bar{K}}^T = (\,-\dot{\chi}_\tau\sin\gamma_\tau \quad \dot{\gamma}_\tau \quad \dot{\chi}_\tau\cos\gamma_\tau\,)_{\bar{K}} \tag{50}$$

The $\bar{K}$ frame is obtained by rotating the kinematic frame around the x_K axis by μ_k such that the $y_{\bar{K}}$ axis is in the tangential plane. Note that in [8] it is assumed that $\gamma_\tau \approx 0$, which is only justified if the reeling-out speed is small compared to the x and y components of the kinematic velocity vector given in the tangential plane frame. Hence, Eq. (50) generalizes the result in [8]. Furthermore, Eq. (50) offers through $\dot{\gamma}_\tau$ another control degree of freedom that can be used to assist the winch controller in the radial direction motion control. In this work this has not been further investigated, and hence $\dot{\gamma}_{\tau,c}$ is set to zero.

$(\boldsymbol{\omega}^{\tau\bar{K}})_{\bar{K}}$ can be converted into the angular velocity vector between the O and $\bar{K}$ frame, denoted with $(\boldsymbol{\omega}^{O\bar{K}})_{\bar{K}}$ according to

$$(\boldsymbol{\omega}^{O\bar{K}})_{\bar{K}} = \boldsymbol{M}_{\bar{K}O}((\boldsymbol{\omega}^{OW})_O + \boldsymbol{M}_{OW}(\boldsymbol{\omega}^{W\tau})_W) + (\boldsymbol{\omega}^{\tau\bar{K}})_{\bar{K}} \tag{51}$$

It is reasonable to assume that the mean wind direction changes much slower than the transport rate $(\boldsymbol{\omega}^{W\tau})_W$ and the course rate vector $(\boldsymbol{\omega}^{\tau\bar{K}})_{\bar{K}}$; hence $(\boldsymbol{\omega}^{OW})_K$ can be set to zero. This yields

$$\begin{aligned}(\boldsymbol{\omega}^{O\bar{K}})_{\bar{K}} &= \boldsymbol{M}_{\bar{K}O}\boldsymbol{M}_{OW}(\boldsymbol{\omega}^{W\tau})_W + (\boldsymbol{\omega}^{\tau\bar{K}})_{\bar{K}}\\ &= \begin{pmatrix}\dot{\mu}_k - \dot{\chi}_{k,c}\sin\gamma_k\\ \dot{\gamma}_{k,c}\cos\mu_k + \dot{\chi}_{k,c}\sin\mu_k\cos\gamma_k\\ -\dot{\gamma}_{k,c}\sin\mu_k + \dot{\chi}_{k,c}\cos\mu_k\cos\gamma_k\end{pmatrix}_{\bar{K}}\end{aligned} \tag{52}$$

with

$$(\boldsymbol{\omega}^{W\tau})_W^T = (\,\dot{\phi}\sin\lambda \quad -\dot{\phi}\cos\lambda \quad \dot{\lambda}\,)_W \tag{53}$$

Note that the second equality in Eq. (52) is a generic expression that can be obtained from the literature (for instance, from [14] p. 75). The transformation matrix $\boldsymbol{M}_{\bar{K}O}$ can be calculated using the knowledge of course and path angle as well as the position of the aircraft in the W frame. With

$$\dot{\chi}_{\tau,\parallel} = \frac{(\,\cos(\chi_{\tau,\parallel}) \quad -\sin(\chi_{\tau,\parallel})\,)\begin{pmatrix}((\partial\boldsymbol{e}_{y,\tau}/\partial\lambda)\dot{\lambda} + (\partial\boldsymbol{e}_{y,\tau}/\partial\phi)\dot{\phi})\cdot\boldsymbol{t}^G + \boldsymbol{e}_{y,\tau}\cdot(d\boldsymbol{t}^G/ds)\dot{s}\\ ((\partial\boldsymbol{e}_{x,\tau}/\partial\lambda)\dot{\lambda} + (\partial\boldsymbol{e}_{x,\tau}/\partial\phi)\dot{\phi})\cdot\boldsymbol{t}^G + \boldsymbol{e}_{x,\tau}\cdot(d\boldsymbol{t}^G/ds)\dot{s}\end{pmatrix}}{\|\boldsymbol{t}^G\|} \tag{47}$$

with

$$\boldsymbol{e}_{x,\tau} = \begin{pmatrix}-\sin\phi\cos\lambda\\ -\sin\phi\sin\lambda\\ \cos\phi\end{pmatrix}, \qquad \boldsymbol{e}_{y,\tau} = \begin{pmatrix}-\sin\lambda\\ \cos\lambda\\ 0\end{pmatrix} \tag{48}$$

and

$$\dot{\lambda} = \frac{v_k^G}{\|(\boldsymbol{p}^G)_W\|\cos\phi}, \qquad \dot{\phi} = \frac{u_k^G}{\|(\boldsymbol{p}^G)_W\|} \tag{49}$$

$$\boldsymbol{e}_{x,\bar{K},O} = \begin{pmatrix}\cos\chi_k\cos\gamma_k\\ \sin\chi_k\cos\gamma_k\\ -\sin\gamma_k\end{pmatrix} \quad \boldsymbol{e}_{y,\bar{K},O} = \frac{-\boldsymbol{M}_{OW}(\boldsymbol{p}^G)_W\times\boldsymbol{e}_{x,\bar{K},O}}{\|-\boldsymbol{M}_{OW}(\boldsymbol{p}^G)_W\times\boldsymbol{e}_{x,\bar{K},O}\|}$$
$$\boldsymbol{e}_{z,\bar{K},O} = \boldsymbol{e}_{x,\bar{K},O}\times\boldsymbol{e}_{y,\bar{K},O} \tag{54}$$

this yields

$$\boldsymbol{M}_{\bar{K}O} = \begin{pmatrix}\boldsymbol{e}_{x,\bar{K},O}^T\\ \boldsymbol{e}_{y,\bar{K},O}^T\\ \boldsymbol{e}_{z,\bar{K},O}^T\end{pmatrix} \tag{55}$$

Ultimately, the desired course and path angle rates can be calculated according to

$$\dot{\chi}_{k,c} = \frac{\omega_{y,\bar{K}}^{O\bar{K}} \sin\mu_k + \omega_{z,\bar{K}}^{O\bar{K}} \cos\mu_k}{\cos\gamma_k} \quad \dot{\gamma}_{k,c} = \omega_{y,\bar{K}}^{O\bar{K}} \cos\mu_k - \omega_{z,\bar{K}}^{O\bar{K}} \sin\mu_k \tag{56}$$

with

$$\mu_k = \arctan\left(\frac{M_{\bar{K}O,23}}{M_{\bar{K}O,33}}\right) \tag{57}$$

The block diagram of the guidance module and the course controller is depicted in Fig. 17.

2. Retraction Phase Guidance

The retraction phase guidance module is separated from the traction phase module. The supervisory logic switches to the retraction phase according to the high-level state machine status. The outputs of the retraction guidance module are again course and path angle commands. In contrast to the traction phase the aircraft will not follow a prescribed path but directly flies toward the zenith position with a predefined path angle. The path angle set point is given by a fixed descend angle, which is chosen manually. The course angle is calculated based on the relative position of the aircraft and the waypoint that is located at the zenith position of the small Earth. The choice of this waypoint seems natural because reeling in the tether will automatically pull the aircraft toward the zenith position. Additionally, in order to achieve a smoother transition back into the traction phase a *flare-like* maneuver is commanded that increases the descent rate linearly, leading to a slight pull-up maneuver before the aircraft goes back into cross wind flight. The flare is initiated as a function of the aircraft latitude:

$$\gamma_{k,c} = \frac{\gamma_f - \gamma_i}{\phi_{\max} - \phi_0}(\phi - \phi_0) + \gamma_i \quad \bar{\gamma}_{k,c} = \max(\min(\gamma_{k,c}, \gamma_f), \gamma_i) \tag{58}$$

with $\phi_0 = \phi_{\max} - \Delta\phi$. The parameters $\Delta\phi, \gamma_f, \gamma_i$ are chosen manually by the operator and characterize the length of the flare, in terms of elevation angle, as well as the final and initial descent angle. The desired course angle is calculated based on the relative position of the aircraft and the origin of the wind frame:

$$\boldsymbol{b}_O^T = -(\, p_{O,x} \quad p_{O,y} \quad 0\,) \tag{59}$$

The course set point is then given by

$$\chi_{k,c} = \arctan_2(b_{O,y}, b_{O,x}) \tag{60}$$

C. Path Loop

1. Traction Phase

In the path loop the commanded course and path angle as well as their corresponding rates (output of guidance module) are used to calculate the set points for the attitude loop, as depicted in the block diagram in Fig. 18. The overall pseudo control inputs are given by

$$\begin{aligned}\nu_\chi &= \dot{\chi}_{k,c} + k_{p,\chi}(\chi_{k,c} - \chi_k) + k_{i,\chi}\int_0^t (\chi_{k,c} - \chi_k)\,\mathrm{d}\tau \\ \nu_\gamma &= \dot{\gamma}_{k,c} + k_{p,\gamma}(\gamma_{k,c} - \gamma_k) + k_{i,\gamma}\int_0^t (\gamma_{k,c} - \gamma_k)\,\mathrm{d}\tau\end{aligned} \tag{61}$$

The set points of the attitude controller will be derived using a model for the path dynamics. The total acceleration of the aircraft in the kinematic frame is given by:

$$(\dot{\boldsymbol{v}}_k)_K^O = \begin{pmatrix}\dot{v}_k \\ 0 \\ 0\end{pmatrix}_K + (\boldsymbol{\omega}^{OK})_K \times \begin{pmatrix}v_k \\ 0 \\ 0\end{pmatrix}_K = \begin{pmatrix}\dot{v}_k \\ \dot{\chi}_k \cos\gamma_k v_k \\ -\dot{\gamma}_k v_k\end{pmatrix}_K = \begin{pmatrix}a_{x,K} \\ a_{y,K} \\ a_{z,K}\end{pmatrix}_K \tag{62}$$

The path dynamic are then defined according to

$$m\begin{pmatrix}a_{x,K} \\ a_{y,K} \\ a_{z,K}\end{pmatrix}_K = (\boldsymbol{F}_a)_K + (\boldsymbol{F}_g)_K + (\boldsymbol{F}_t)_K \tag{63}$$

involving the aerodynamic force $(\boldsymbol{F}_a)_K \in \mathbb{R}^{3\times1}$, gravitational force $(\boldsymbol{F}_g)_K \in \mathbb{R}^{3\times1}$, as well as the tether force $(\boldsymbol{F}_t)_K \in \mathbb{R}^{3\times1}$ in the K frame, where gravity and tether force are calculated with

$$(\boldsymbol{F}_g)_K^T = (\,-\sin\gamma_k m_k g \quad 0 \quad \cos\gamma_k m_k g\,) \tag{64}$$

and

$$(\boldsymbol{F}_t)_K = -\boldsymbol{M}_{KO}\frac{(\boldsymbol{p})_O}{\|(\boldsymbol{p})_O\|_2}F_t \tag{65}$$

Solving for the aerodynamic force yields

$$\begin{pmatrix}f_{x,a,K} \\ f_{y,a,K} \\ f_{z,a,K}\end{pmatrix}_K = m\begin{pmatrix}a_{x,K} \\ a_{y,K} \\ a_{z,K}\end{pmatrix}_K - (\boldsymbol{F}_g)_K - (\boldsymbol{F}_t)_K = (\boldsymbol{F}_a)_K \tag{66}$$

The last two rows can be written as

$$\begin{aligned}f_{y,a,K} &= \cos\mu_k f_{a,y,\bar{K}} - \sin\mu_k f_{a,z,\bar{K}} \\ f_{z,a,K} &= \sin\mu_k f_{a,y,\bar{K}} + \cos\mu_k f_{a,z,\bar{K}}\end{aligned} \tag{67}$$

where μ_k is the kinematic bank angle, that is, the roll angle around the kinematic velocity vector and

$$\begin{aligned}f_{a,y,\bar{K}} &= -\cos\alpha_k \sin\beta_k f_{a,x,B} + \cos\beta_k f_{a,y,B} - \sin\alpha_k \sin\beta_k f_{a,z,B} \\ f_{a,z,\bar{K}} &= -\sin\alpha_k f_{a,x,B} + \cos\alpha_k f_{a,z,B}\end{aligned} \tag{68}$$

Note that α_k and β_k are the kinematic angle of attack and kinematics sideslip angle. Because the inner loop controller actively controls the sideslip angle β (i.e., the aerodynamic sideslip angle), the aerodynamic side force $f_{a,y,B}$ is approximately zero. Contrarily, the kinematic sideslip angle β_k is in the presence of wind not zero. Hence,

$$\begin{aligned}f_{a,y,\bar{K}} &= -\cos\alpha_k \sin\beta_k f_{a,x,B} - \sin\alpha_k \sin\beta_k f_{a,z,B} \\ f_{a,z,\bar{K}} &= -\sin\alpha_k f_{a,x,B} + \cos\alpha_k f_{a,z,B}\end{aligned} \tag{69}$$

The set point for the kinematic bank angle based on the required course and path angle rate is calculated by solving Eq. (67) for μ_k and inserting the pseudo control signals for the course and path angle rates:

$$\begin{aligned}\mu_{k,c} = \arctan_2&\left(\frac{m_k \nu_\chi \cos\gamma_k v_k - f_{t,y,K}}{m_k \nu_\gamma v_k + m_k g\cos\gamma_k + f_{t,z,K}}\right) \\ &+ \arctan\left(\frac{f_{a,y,\bar{K}}}{f_{a,z,\bar{K}}}\right)\end{aligned} \tag{70}$$

which requires estimates for the aerodynamic forces $f_{a,y,\bar{K}}$ and $f_{a,z,\bar{K}}$.

Based on the set point for the kinematic banking angle the corresponding Euler roll angle can be calculated according to

$$\Phi_c = \arcsin\left(\frac{\cos\gamma_k \cos\beta_k(\sin\mu_{k,c} - \tan\gamma_k \tan\beta_k)}{\cos\Theta}\right) \tag{71}$$

Equation (71) can be obtained by comparing the relevant coefficients of $\boldsymbol{M}_{B\tau} = \boldsymbol{M}_{BO}\boldsymbol{M}_{OW}\boldsymbol{M}_{W\tau}$. The matrix $\boldsymbol{M}_{BO}$ is obtained, for instance, from ([12] p. 12). The matrix $\boldsymbol{M}_{W\tau}$ is equivalent to the transformation from the Earth-Centered-Earth-Fixed (E) frame into the O frame (see [12] p. 31) where the E frame corresponds to the W frame and the O frame corresponds to the τ frame. $\boldsymbol{M}_{OW}$ is given by

$$\boldsymbol{M}_{OW} = \begin{pmatrix} \cos\xi & \sin\xi & 0 \\ \sin\xi & -\cos\xi & 0 \\ 0 & 0 & -1 \end{pmatrix} \tag{72}$$

where ξ denotes the wind direction measured from the north direction. Note that the structure of $\boldsymbol{M}_{B\tau}$ is equivalent to the structure of $\boldsymbol{M}_{BO}$. Φ_c can then be transformed into an aerodynamic banking angle command $\mu_{a,c}$ using Eq. (73).

$$\mu_{a,c} = \arcsin\left(\frac{\cos\Theta \sin\Phi_c}{\cos\gamma_a \cos\beta} + \tan\gamma_a \tan\beta\right) \tag{73}$$

The required aerodynamic path angle can be calculated using Eq. (74), which has been derived in ([13] pp. 20–23).

$$\gamma_a = \arcsin\left(\frac{v_k \sin\gamma_k + v_{w,O,z}}{v_a}\right) \approx \arcsin\left(\frac{v_k \sin\gamma_k}{v_a}\right) \tag{74}$$

Notice that the calculation of γ_a requires the knowledge of the wind component in z_O direction $v_{w,O,z}$, which is, however, usually negligibly small compared with the horizontal components. The angle of attack set point can be calculated similarly to the approach presented in [25] with

$$L_{\text{req}} \approx \sqrt{\bar{f}_{y,K}^2 + \bar{f}_{z,K}^2} \tag{75}$$

Note that, due to the wind influence, this is only an approximation, which is neglected in [25]. However, because the available traction force needs to be maximized it makes sense to choose a fixed set point during the traction phase close to the maximum angle of attack. Setting the angle of attack to a fixed value is similar to the case where the angle of attack saturates. This can lead to a windup of the integrators in the path loop. One approach to mitigate the windup is to adapt the reference model by the control deficit that results from the saturation (i.e., pseudo control hedging, PCH). However, for the traction phase controller the reference course rate is directly calculated based on the path geometry, as discussed in the previous section. This prevents a standard implementation of PCH, because no reference filter is used. Instead, an anti-windup scheme based on *back-calculation* is used, where the feedback part corresponds to the deficit between, for instance, the commanded course rate $\nu_{\chi,k,c}$ and the expected course rate $\hat{\dot{\chi}}_{k,c}$. The hedge signal is in this case defined by

$$\nu_{h,\chi} = k_{bc}(\nu_{\chi,k,c} - \hat{\dot{\chi}}_{k,c}) \tag{76}$$

The gain k_{bc} is chosen to be smaller than the integrator gain, as recommended in ([26] pp. 79–80). The feedback law for the pseudo control input is then adapted according to

$$\nu_\chi = \dot{\chi}_{k,c} + k_{p,\chi}(\chi_{k,c} - \chi_k) \quad + k_{i,\chi}\int_0^t (\chi_{k,c} - \chi_k - \nu_{h,\chi})\,\mathrm{d}\tau \tag{77}$$

The adaption of the flight path rate channel follows analogously.

2. Retraction Phase

For the retraction phase the course and path angle controller are designed similarly to the traction phase controller; the only difference consists of the calculation of the course and path angle rate commands. Because in the retraction phase no defined path needs to be followed, the rate commands are generated with second-order reference filters. Although first-order filters would be sufficient, second-order filters lead to an additional smoothing of the derivatives [27]. Instead of using a back-calculation anti-windup scheme a conventional PCH approach is chosen using estimates for the feasible course and path angle rates. With the hedging signal ν_h the equations of the second-order filter, here displayed for the course filter, are defined by

$$\dot{\nu}_{r,\chi} = -2\zeta\omega_0\nu_{r,\chi} + \omega_0^2(\chi_{k,c} - \chi_{k,r}) \quad \dot{\chi}_{k,r} = \nu_{r,\chi} - \nu_h \tag{78}$$

and an equivalent pseudo control law with PI controller as for the traction phase is used [see Eq. (61)]. Note that, in contrast to a fixed value for the angle of attack set point, the approximate expression of the required lift in Eq. (75) is used to determine the corresponding lift coefficient and by inversion of the lift coefficient the angle of attack set point α_c for the attitude loop is determined.

D. Attitude Loop

The pseudo-control inputs for the attitude to rate inversion are given by

$$\begin{aligned} \nu_{\mu_a} &= \nu_{r,\mu_a} + K_{\mu,p}(\mu_{a,r} - \mu_a) + K_{\mu,i}\int_0^t (\mu_{a,r} - \mu_a)\,\mathrm{d}\tau \\ \nu_\alpha &= \nu_{r,\alpha} + K_{\alpha,p}(\alpha_r - \alpha) + K_{\alpha,i}\int_0^t (\alpha_r - \alpha)\,\mathrm{d}\tau \\ \nu_\beta &= K_{\beta,p}(\beta_r - \beta) + K_{\beta,i}\int_0^t (\beta_r - \beta)\,\mathrm{d}\tau \end{aligned} \tag{79}$$

where ν_{r,μ_a} and $\nu_{r,\alpha}$ are calculated with an equivalent reference filter as defined for the course angle in Eq. (78). The inversion of the attitude to rate dynamics is purely kinematic and given by

$$(\boldsymbol{\omega}_c^{OB})_B = \boldsymbol{M}_{B\bar{A}}\begin{pmatrix} -\dot{\chi}_a \sin\gamma_a \\ \dot{\gamma}_a \\ \dot{\chi}_a \cos\gamma_a \end{pmatrix}_{\bar{A}} + (\boldsymbol{\omega}^{\bar{A}B})_B \tag{80}$$

with

$$(\boldsymbol{\omega}^{\bar{A}B})_B = \begin{pmatrix} \cos\alpha\cos\beta\nu_\mu + \nu_\beta \sin\alpha \\ \sin\beta\nu_\mu + \nu_\alpha \\ \sin\alpha\cos\beta\nu_\mu - \cos\alpha\nu_\beta \end{pmatrix}_B \tag{81}$$

The matrix $\boldsymbol{M}_{\bar{A}B}$ is defined, for instance, in ([14] p. 62). $\dot{\chi}_a$ and $\dot{\gamma}_a$ are estimated by filtering Eqs. (74) and (82), as derived in ([13] p. 23)

$$\begin{aligned} \chi_a = \chi_k + \beta - \arcsin\Bigg(&\frac{1}{V_a\cos\gamma_a}(v_{w,O,y}\cos\chi_{k,c} \\ &- v_{w,O,x}\sin\chi_{k,c})\Bigg) \end{aligned} \tag{82}$$

using a washout-filter, as proposed in [28]:

$$G(s) = \frac{s\omega_f^2}{s^2 + 2\omega_f s + \omega_f^2} \tag{83}$$

where $\omega_f = 90\ \text{rad}\cdot\text{s}^{-1}$ is the chosen filter bandwidth. Note that a better accuracy could be achieved by calculating $\dot{\chi}_k$ and $\dot{\gamma}_k$ analytically using the model of the course and path rate dynamics as defined in Eq. (63) and only filter the remaining terms. Alternatively, a model can be used to estimate $\dot{\chi}_a$ and $\dot{\gamma}_a$, which requires to write down the path dynamics with respect to the aerodynamic frame assuming a stationary wind field.

E. Rate Loop

Note that because it is assumed that the tether is connected close to the center of gravity of the aircraft the rate loop of the tethered aircraft can be implemented analogously to the rate loop of a conventional aircraft. In the literature there exists an ample amount of different approaches to control the rate dynamics of aircraft; in this work a conventional first-order dynamic inversion controller with second-order reference filters and an incremental control allocation as presented in [25] is used. Note that the incremental approach is necessary because in general the relationship between actuator inputs and aerodynamic moments is nonlinear and not globally invertible. Because up to now and in the future extensive effort is and will be put into the modeling and identification of the AWE system, a model-based inversion is chosen over a sensor-based inversion as, for instance, presented in [29].

The commanded attitude rates as calculated by Eq. (80) are filtered and the resulting rate accelerations are added to a PI control part analogously to Eq. (79), yielding the pseudo-control input ν_ω for the inversion of the rate dynamics as defined in Eq. (4). From the resulting moment the current acting moment on the aircraft, estimated using a model, is subtracted, yielding the required moment increment to track the commanded rates:

$$\begin{pmatrix} \Delta L \\ \Delta M \\ \Delta N \end{pmatrix} = \begin{pmatrix} L_c \\ M_c \\ N_c \end{pmatrix} - \begin{pmatrix} L_0 \\ M_0 \\ N_0 \end{pmatrix} = \boldsymbol{J}\nu_\omega + (\boldsymbol{\omega}^{OB})_B \times \boldsymbol{J}(\boldsymbol{\omega}^{OB})_B - \begin{pmatrix} L_0 \\ M_0 \\ N_0 \end{pmatrix} \tag{84}$$

The block diagram of the rate loop is depicted in Fig. 19.

F. Control Allocation

Eventually, the moment increments are mapped to a surface deflection increment that is added to the current surface deflection, resulting in the final actuator command:

$$\begin{pmatrix} \delta_{a,c} \\ \delta_{e,c} \\ \delta_{r,c} \end{pmatrix} = \begin{pmatrix} \delta_{a,0} \\ \delta_{e,0} \\ \delta_{r,0} \end{pmatrix} + \begin{pmatrix} \Delta\delta_a \\ \Delta\delta_e \\ \Delta\delta_r \end{pmatrix} = \begin{pmatrix} \delta_{a,0} \\ \delta_{e,0} \\ \delta_{r,0} \end{pmatrix} + \begin{pmatrix} C_{l\delta_a} & 0 & C_{l\delta_r} \\ 0 & C_{m\delta_e} & 0 \\ C_{n\delta_a} & 0 & C_{n\delta_r} \end{pmatrix}^{-1} \begin{pmatrix} \Delta L \\ \Delta M \\ \Delta N \end{pmatrix} \tag{85}$$

where the $C_{i,j}$ coefficients represent roll- (L), pitch- (M), or yaw-moment (N) control derivatives that are obtained by linearizing the aerodynamic moment model with respect to the control surface deflections.

G. Winch Controller

The winch controller is derived based on the model defined in Eq. (9) without explicitly taking into account the aircraft dynamics as presented, for instance, in [30]. The reason is that, if the aircraft dynamics are taken into account, the full state vector of the aircraft needs to be available to the winch controller, including a tether model with measurable states. So far no reliable information about the communication between the aircraft and the ground station is available and feedback of tether states is not practical. Hence, it is decided to control the winch only based on the measured tether force on the ground. In AWE, two high-level control objectives for the winch controller can be formulated. First, the net power output has to be maximized by controlling the radial motion of the aircraft in an optimal way; second, the winch controller needs to prevent too high tension in the tether, for instance, as a result of sudden wind speed changes, which would lead to a tether rupture or damage of the aircraft. In this work, the focus is on the second control objective, because it is more critical for the reliable operation of the AWE system.

Note that, from the perspective of the winch, the dynamics of the aircraft and the tether represent a disturbance that the winch controller needs to regulate in order to track a force set point. If a tether force measurement on the ground is available, which is usually the case in this application, a complex disturbance model is not necessary because all relevant information is condensed in the force measurement. Note that this approach assumes implicitly that the difference between the tether force measured on the ground and the tether force measured at the aircraft is negligible. Simulation results show that this assumption is valid during the traction phase. The set point for the reeling speed can be derived as follows. The aircraft dynamics in the tangential plane, or spherical coordinates, are given by

$$(\dot{\boldsymbol{v}}^G)_\tau + (\boldsymbol{\omega})_\tau^{W\tau} \times (\boldsymbol{v}^G)_\tau = \frac{(\boldsymbol{F}_g)_\tau + (\boldsymbol{F}_a)_\tau + (\boldsymbol{F}_t)_\tau}{m_k} \tag{86}$$

Assuming a straight tether only, the third row is relevant, which is given by

$$\dot{v}_{z,\tau} = -\omega_x v_{y,\tau} + \omega_y v_{x,\tau} + \frac{F_{g,z,\tau} + F_{a,z,\tau} + F_t}{m_k} \tag{87}$$

This can be written more compactly as

$$\dot{v}_{z,\tau} = \frac{F_{\text{aircraft}} + F_t}{m_k} \tag{88}$$

with

$$F_{\text{aircraft}} = m_k(-\omega_x v_{y,\tau} + \omega_y v_{x,\tau}) + F_{g,z,\tau} + F_{a,z,\tau} \tag{89}$$

Note that F_{aircraft} requires the knowledge of the full aerodynamic model of the aircraft as well as the relevant measured states if used for the set point calculation. However, instead of an estimation of F_{aircraft} the measured tether force on the ground can be used if it is assumed that $F_{\text{aircraft}} \approx -F_{t,m}$. If the tether is straight, the reeling speed v_r is equal to $-v_{z,\tau}$; hence

$$\dot{v}_r = \frac{F_{t,m} - F_t}{m_k} \tag{90}$$

If F_t is replaced by the desired traction force $F_{t,c}$ the resulting acceleration can be interpreted as a reference acceleration proportional to the tether force tracking error. With $\dot{\omega}_w = \dot{v}_r / r_w$ this expression can be substituted into the winch model in Eq. (9) and solved for the reference torque:

$$M_c = \left(\frac{J_w}{r_w m_k} - r_w\right) F_{t,m} - \frac{J_w}{r_w m_k} F_{t,c} \tag{91}$$

Substituting this expression back into the winch model yields the closed-loop winch model

$$\dot{\omega}_w = \frac{1}{r_w m_k}(F_{t,m} - F_{t,c}) + \Delta_w \tag{92}$$

where Δ_w is the model mismatch as a result of an imperfect inversion of the plant dynamics. Note that, if the measured tether force deviates from the set point, the winch will reel out faster or slower. Although simple, this approach proved to be highly effective in dealing with varying wind conditions and wind gusts as will be shown in Sec. IV, while being independent of any aircraft state. To get rid of steady state errors an integrator term $k_i \int_0^t F_m - F_{t,s}\, \mathrm{d}\tau$ can be added to Eq. (91). For the stability of Eq. (92) only a qualitative but intuitive stability proof is given. If the tether force becomes larger than the set point force, the winch will start to accelerate according to Eq. (92). Of course this is

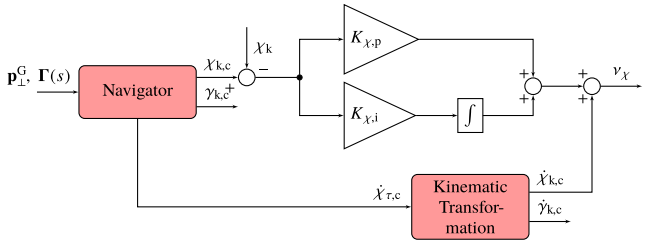

Fig. 17 Guidance module and course controller block diagram.

strictly only true if $(1/r_w m_k)(F_m - F_{t,s}) > \Delta_w$. However, in the opposite case the acceleration will only be delayed, because if the winch further decelerates the tension in the tether would increase steadily until the tracking error contribution will be larger than Δ_w. If the winch accelerates, the kinematic radial speed of the aircraft will increase, which decreases the apparent wind speed. As a consequence the lift force will drop, which decreases the tension in the tether and therefore decreases the tether force tracking error. The causal chain holds of course for the opposite case as well, where the tether force is smaller than the force set point.

During the retraction phase the reeling-in speed is set to a fixed value, usually the maximum reeling-in speed that the winch can achieve, and is chosen in order to minimize the retraction time. For the tracking task of the speed controller a dynamic-model-based feed-forward controller (see [31] pp. 324–328) for fast tracking is combined with a linear quadratic feedback regulator with servomechanism ([32] pp. 51–62). The prefilter is used to create smooth transitions between set point changes. Additionally, a feed-forward disturbance compensation is added because from the perspective of the speed controller the tether force represents a measurable disturbance.

IV. Results

In this section two different simulation campaigns are used to investigate the robustness of the control system. First, the robustness with respect to modest changes in the wind speed due to turbulence and wind shear is assessed. In the second part, the effect on the control performance due to sudden and significant wind speed changes caused by gusts is analyzed.

A. Consecutive Pumping Cycles in a Turbulent Wind Field

Figures 20 and 21 show the resulting flight paths projected into the $x_W z_W$ and $x_W y_W$ planes, respectively. Figure 22 depicts the path

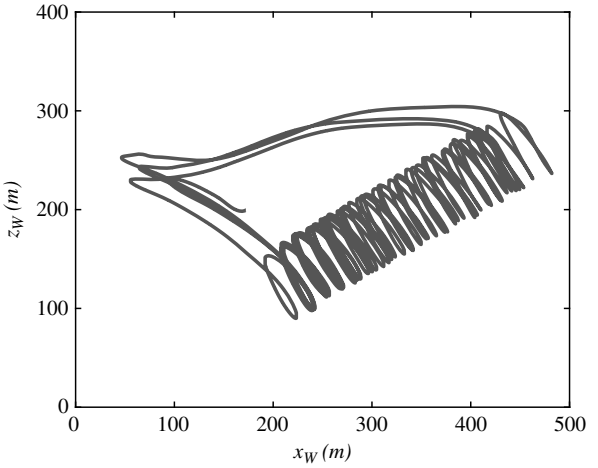

Fig. 20 Flight path in $x_W z_W$ plane.

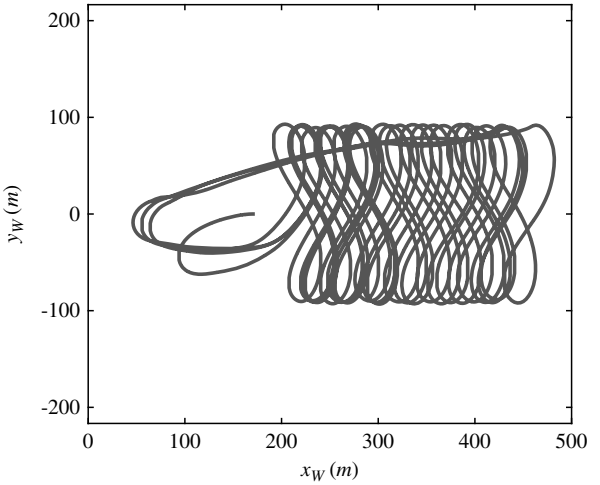

Fig. 21 Flight path in $x_W y_W$ plane.

projected into the tangential plane at $\lambda = 0°$ and $\phi = \phi_0$ (center of the figure of eight). Despite the turbulent wind field, shown in Figs. 23 and 24, the control system is able to guide the aircraft along the defined flight path reliably. The visible deviations between the

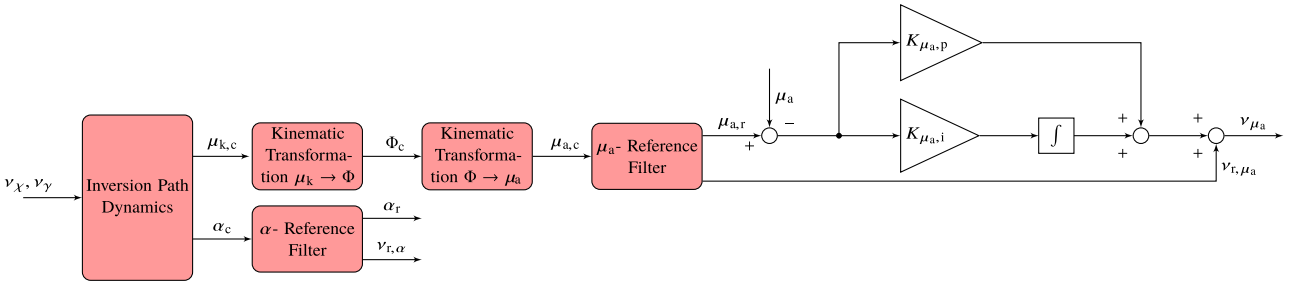

Fig. 18 Path and attitude loop block diagram.

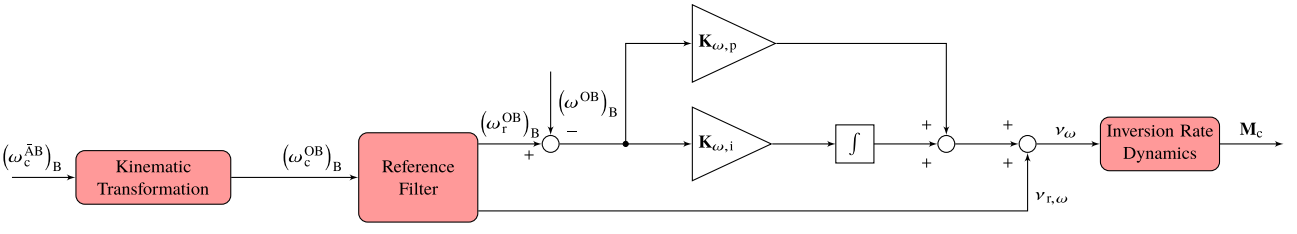

Fig. 19 Rate loop block diagram.

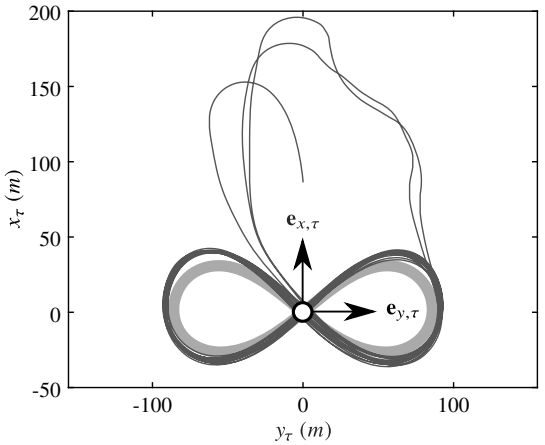

Fig. 22 Figure-of-eight flight path projected into the tangential plane.

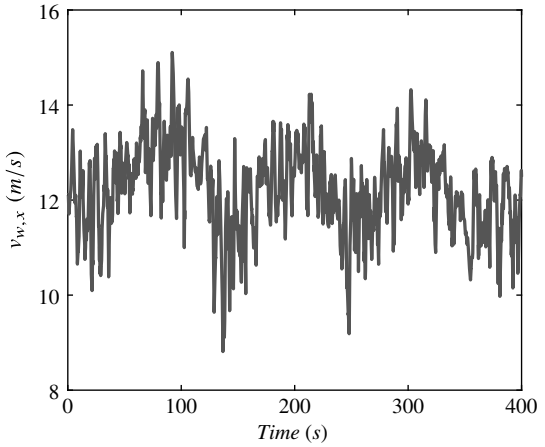

Fig. 23 The x component of the wind velocity vector in the W frame.

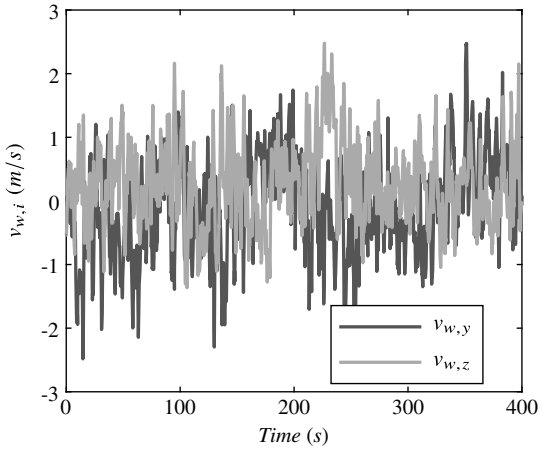

Fig. 24 The y and z components of the wind velocity vector in the W frame.

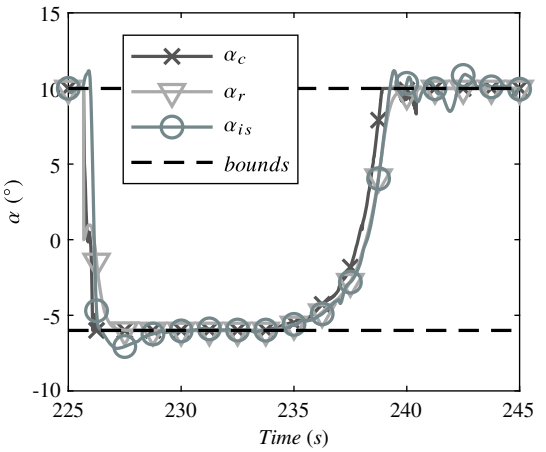

Fig. 25 Angle of attack tracking.

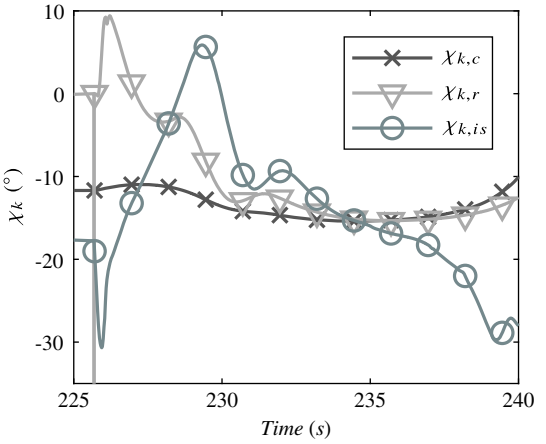

Fig. 26 Course angle tracking during retraction.

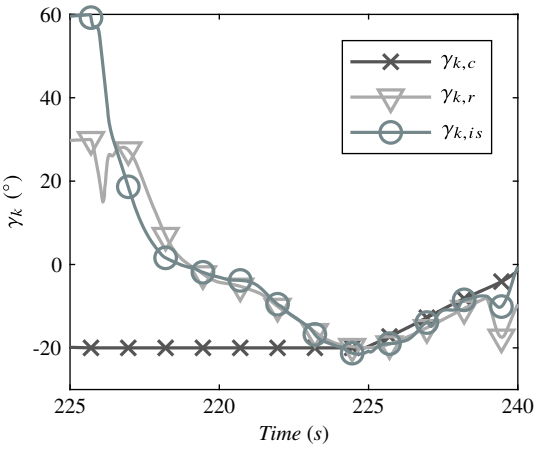

Fig. 27 Flight path angle tracking during retraction.

reference path (light gray curve in Fig. 22) and the real flight path are acceptable and are caused by the limited bandwidth of the control system. This limitation results in a repetitive nonzero cross-track error during the turns. The results display roughly three consecutive pumping cycles. The reoccurring flight pattern demonstrates the robustness of the closed-loop system toward modest changes in wind speed caused by wind shear and turbulence.

As described in Sec. III, reference filters are used to generate the course and path angle rates during the retraction phase. This allows to implement PCH to adapt the reference filters in case of saturation of the control signal. From the point of view of the path loop, the control signals are the bank angle command $\mu_{a,c}$ as well as the angle of attack command α_c. In Fig. 25 it can be observed that, during a significant part of the retraction phase, for instance, between 226 and 234 s, the angle of attack is saturating. In this case the commanded pseudo-control inputs ν_γ and ν_χ will deviate from the actual plant responses. The adaptation of the course and path angle reference filters can be observed in Figs. 26 and 27. The effect is especially visible for the path angle whose primary control variable is the angle of attack. As the angle of attack is saturating the reference path angle increases (e.g., at ≈226 s) as a result of the hedge signal before it decreases

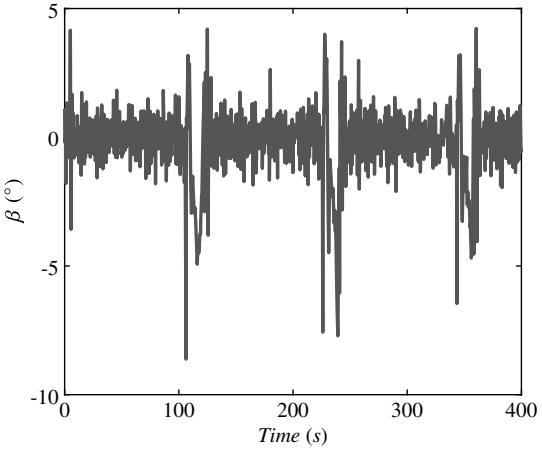

Fig. 28 Sideslip angle regulation.

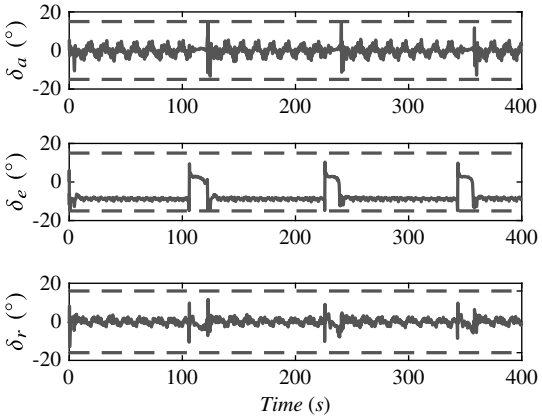

Fig. 29 Control surface deflections with limits (dashed lines).

again and eventually converges toward the negative commanded set point $\gamma_{k,c}$.

During the pumping cycles the sideslip angle varies most of the time between $-2°$ to $+2°$. Larger sideslip angles occur during the transition phases from traction into retraction and vice verse as can be seen in Fig. 28. The evolution of the aircraft control surface deflections is depicted in Fig. 29. It can be observed that the highest control effort is required in the transition phases where the control surfaces partially saturate. During the traction phases the aileron δ_a and rudder δ_r inputs vary in a repetitive manner between $-5°$ to $+5°$, whereas the elevator deflection δ_e remains almost constant at around $-9°$ as a result of the fixed angle of attack set point during the traction phase.

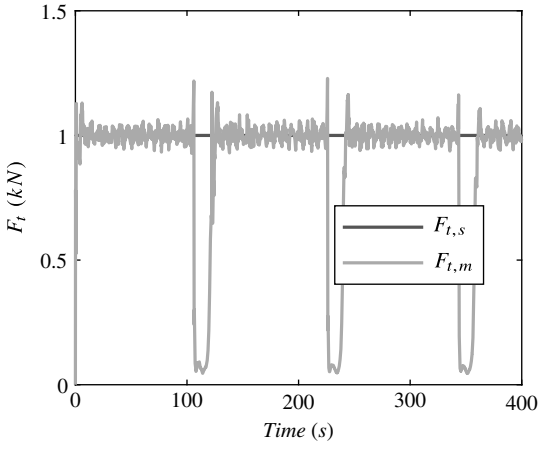

Fig. 30 Tether force tracking.

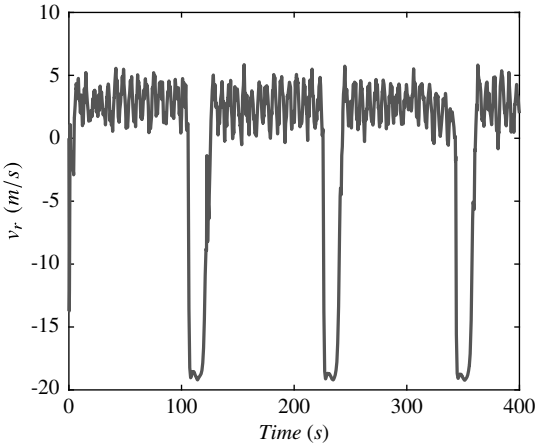

Fig. 31 Reeling speed.

Besides the analysis of the flight control performance the winch control performance needs to be assessed. Figure 30 shows the evolution of the tether force as measured on the ground. During the conducted simulations a tether force set point of 1000 N is chosen, which is well beyond the structural limitations of around 1500 N. The tether force oscillates around the set point with an amplitude of around 50–100 N. The oscillations are a result of the continues acceleration and deceleration of the aircraft while flying down and upward during the figure-of-eight flight patterns. To further reduce these oscillations an improved feed-forward winch controller could be implemented in the future that systematically reels out slower during upward and faster during downward flight. At the moment this

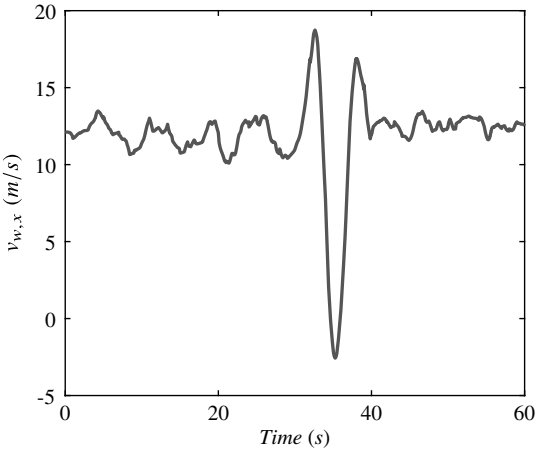

Fig. 32 Gust in upwind direction.

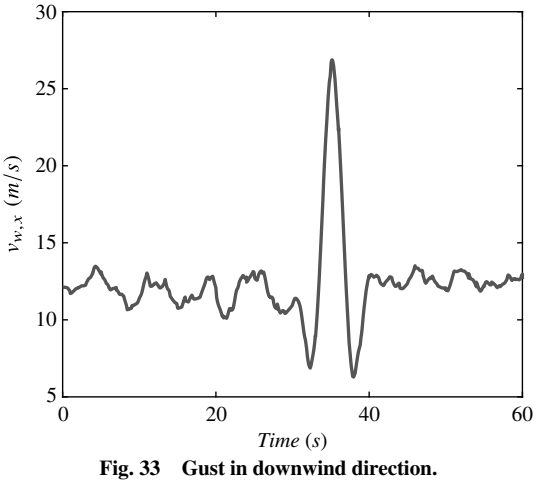

Fig. 33 Gust in downwind direction.

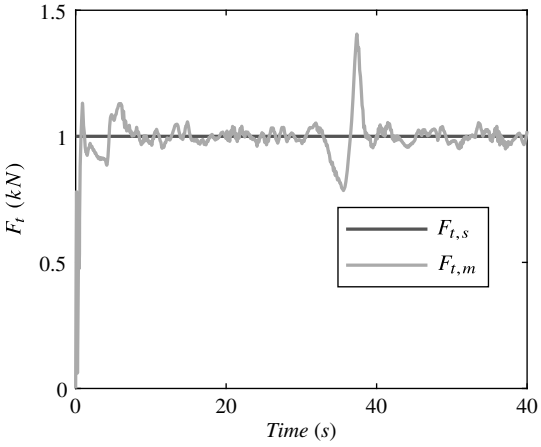

Fig. 34 Tether force with gust in upwind direction.

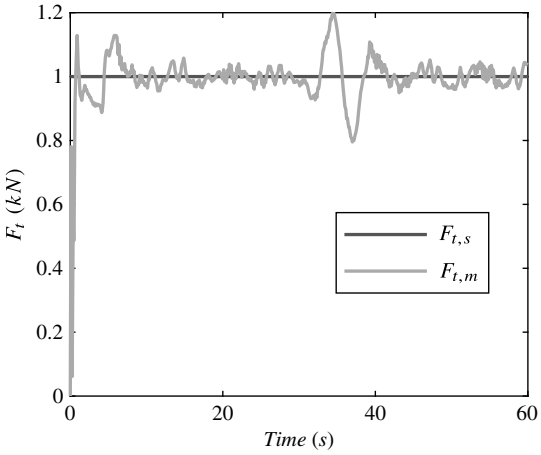

Fig. 35 Tether force with gust in downwind direction.

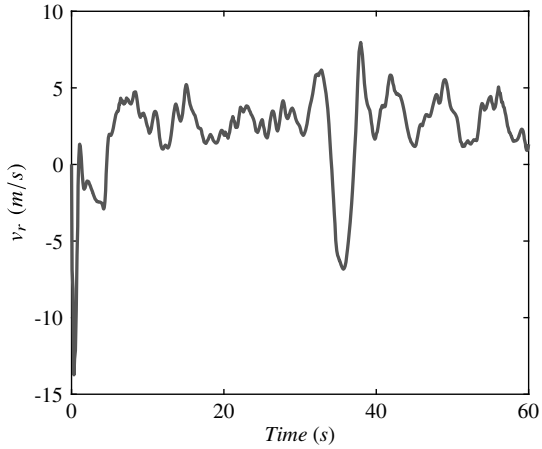

Fig. 36 v_r with gust in upwind direction.

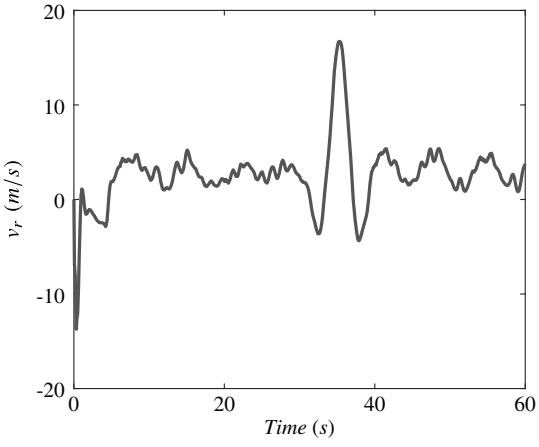

Fig. 37 v_r with gust in downwind direction.

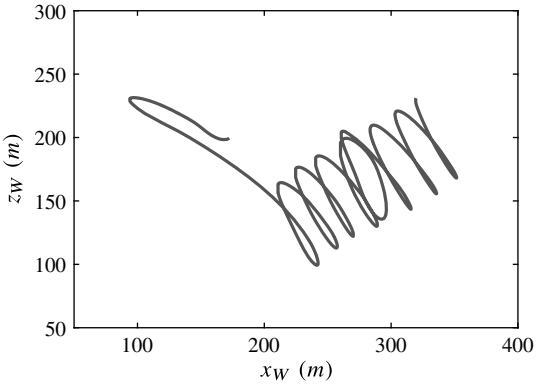

Fig. 38 Flight path with gust in upwind direction.

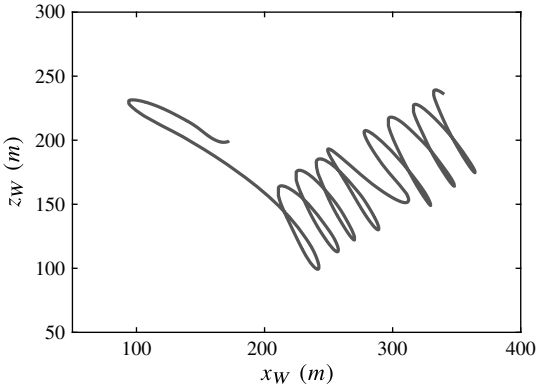

Fig. 39 Fight path with gust in downwind direction.

is partially achieved via feedback control of the tether force. Furthermore, the resulting variations in the reeling speed depicted in Fig. 31 should be reduced in the future because variations in reeling speed would lead to large oscillations in the mechanical power output in combination with a constant tether force. One option to tackle this problem would be to use the pitch channel of the aircraft to control the airspeed, which is out of the scope of this paper.

B. Robustness Toward Wind Gusts

In this section the robustness of the control system toward rapid changes in the mean wind speed will be analyzed. For that purpose a *Mexican hat* gust as defined in [33] is implemented and activated during the simulation at a specified instant in time. In this work, only the response of the aircraft toward gusts in up- and downwind directions as depicted in Figs. 32 and 33 is analyzed. In both cases the gust leads to a significant increase or decrease in airspeed and therefore tether force (see Figs. 34 and 35). To keep the tether force around the set point the winch controller has to adapt the reeling out speed according to Eq. (91) (see Figs. 36 and 37). It can be observed that the reeling speed change follows the shape of the gust proportionally. The adaptation of the reeling speed has a direct effect on the flight path in radial direction. The flight path gets either compressed (Fig. 38) or stretched (Fig. 39) depending on the gust direction as a result of the increasing or decreasing reeling out velocity. Contrarily, Figs. 40 and 41 show that the adaptation of the reeling speed has only a small effect on the path-following performance in the tangential plane.

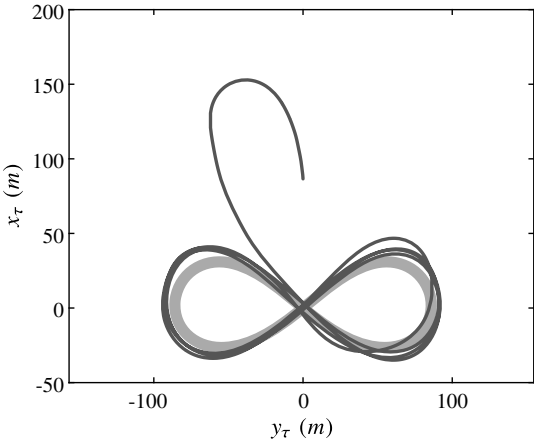

Fig. 40 Flight path with gust in upwind direction.

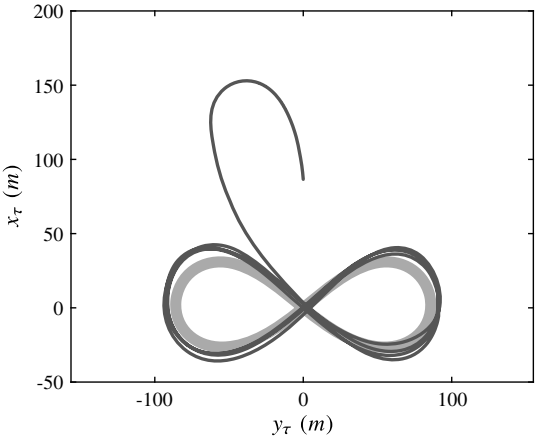

Fig. 41 Fight path with gust in downwind direction.

V. Conclusions

In this paper a novel cascaded-model-based control architecture for rigid wing airborne wind energy systems operated in pumping cycle mode has been presented. The proposed control approach leads to a robust control performance while flying in a realistic turbulent wind field. The extended geometric path-following approach guided the aircraft along a three-dimensional curve reliably. State and input constraints are systematically handled using pseudo control hedging, which turns out to be beneficial especially during the retraction phase where the commanded flight path is adapted automatically in case of angle of attack saturation. Challenging phases during the pumping cycle are the transitions from the traction to the retraction phase and vice versa. Because of the rapid tether force changes in these phases, overshoots in sideslip angle and angle of attack are present although these peaks occurred only for a short period of time and the resulting tracking errors could be regulated back to the set point by the respective feedback controller. Moreover, the results show that the tether force set point can be tracked effectively by directly calculating a torque command as a function of the force tracking error. However, the excellent tether force tracking performance leads to a high variance in the reeling speed and therefore to oscillations in the mechanical power output. This effect could be reduced in the future by additionally using the pitch angle of the aircraft to control the airspeed. In return, this would lead to a less aggressive reeling speed adaption and hence a reduced variance of the mechanical power. In addition to the ability of tracking a constant tether force the proposed winch controller can react to sudden wind speed changes, such as gusts, through adaption of the reeling-out speed, effectively, ensuring the structural integrity of the aircraft.

Acknowledgments

This research has been supported financially by the project AWESCO (H2020-ITN-642682), funded by the European Union's Horizon 2020 research and innovation program under the Marie Sklodowska-Curie grant agreement No. 642682. The authors would like to thank the team of Kitemill AS for supporting this work, in particular Sture Smidt for carrying out the CFD and XFLR5 analysis of the aircraft.

References

[1] Ahrens, U., Diehl, M., and Schmehl, R. (eds.), *Airborne Wind Energy*, Springer, Berlin, 2013. doi:10.1007/978-3-642-39965-7

[2] Schmehl, R. (ed.), *Airborne Wind Energy—Advances in Technology Development and Research*, Springer, Singapore, 2018. doi:10.1007/978-981-10-1947-0

[3] Cherubini, A., Papini, A., Vertechy, R., and Fontana, M., "Airborne Wind Energy Systems: A Review of the Technologies," *Renewable and Sustainable Energy Reviews*, Vol. 51, Nov. 2015, pp. 1461–1476. doi:10.1016/j.rser.2015.07.053

[4] Fechner, U., and Schmehl, R., "Design of a Distributed Kite Power Control System," *Proceedings of the 2012 IEEE International Conference on Control Applications*, IEEE Publ., Piscataway, NJ, 2012, pp. 800–805. doi:10.1109/CCA.2012.6402695

[5] Zgraggen, A. U., Fagiano, L., and Morari, M., "Real-Time Optimization and Adaptation of the Crosswind Flight of Tethered Wings for Airborne Wind Energy," *IEEE Transactions on Control Systems Technology*, Vol. 23, No. 2, 2015, pp. 434–448. doi:10.1109/TCST.2014.2332537

[6] Erhard, M., and Strauch, H., "Flight Control of Tethered Kites in Autonomous Pumping Cycles for Airborne Wind Energy," *Control Engineering Practice*, Vol. 40, July 2015, pp. 13–26. doi:10.1016/j.conengprac.2015.03.001

[7] Fagiano, L., Zgraggen, A. U., Morari, M., and Khammash, M., "Automatic Crosswind Flight of Tethered Wings for Airborne Wind Energy: Modeling, Control Design and Experimental Results," *IEEE Transactions on Control System Technology*, Vol. 22, No. 4, 2014, pp. 1433–1447. doi:10.1109/TCST.2013.2279592

[8] Jehle, C., and Schmehl, R., "Applied Tracking Control for Kite Power Systems," *Journal of Guidance, Control, and Dynamics*, Vol. 37, No. 4, 2014, pp. 1211–1222. doi:10.2514/1.62380

[9] Fagiano, L., Nguyen-Van, E., Rager, F., Schnez, S., and Ohler, C., "Autonomous Takeoff and Flight of a Tethered Aircraft for Airborne Wind Energy," *IEEE Transactions on Control Systems Technology*, Vol. 26, No. 1, 2018, pp. 151–166. doi:10.1109/TCST.2017.2661825

[10] Ilzhöfer, A., Houska, B., and Diehl, M., "Nonlinear MPC of Kites Under Varying Wind Conditions for a New Class of Large-Scale Wind Power Generators," *International Journal of Robust and Nonlinear Control*, Vol. 17, No. 17, 2007, pp. 1590–1599. doi:10.1002/(ISSN)1099-1239

[11] Johnson, E. N., "Limited Authority Adaptive Flight Control," Ph.D. Thesis, Georgia Institute of Technology, Atlanta, GA, 2000, http://hdl.handle.net/1853/12953.

[12] Stevens, B. L., Lewis, F. L., and Johnson, E. N., *Aircraft Control and Simulation*, 3rd ed., Wiley, Hoboken, NJ, 2016. doi:10.1002/9781119174882

[13] Beard, R. W., and McLain, T. W., *Small Unmanned Aircraft: Theory and Practice*, Princeton Univ. Press, Princeton, NJ, 2012. doi:10.1515/9781400840601

[14] Brockhaus, R., Alles, W., and Luckner, R., *Flugregelung*, Springer–Verlag, Berlin, 2011. doi:10.1007/978-3-642-01443-7

[15] Wang, J., "Novel Control Approaches to Quadrotors Inspired by Dynamic Inversion and Backstepping," Ph.D. Thesis, Technical University of Munich, Munich, 2015, https://d-nb.info/107900176X/34.

[16] Fechner, U., van der Vlugt, R., Schreuder, E., and Schmehl, R., "Dynamic Model of a Pumping Kite Power System," *Renewable Energy*, Vol. 83, Nov. 2015, pp. 705–716. doi:10.1016/j.renene.2015.04.028

[17] Calaf, M., Meneveau, C., and Meyers, J., "Large Eddy Simulation Study of Fully Developed Wind-Turbine Array Boundary Layers," *Physics of*

Fluids, Vol. 22, No. 1, 2010, Paper 015110.
doi:10.1063/1.3291077.

[18] Goit, J., and Meyers, J., "Optimal Control of Energy Extraction in Wind-Farm Boundary Layers," *Journal of Fluid Mechanics*, Vol. 768, No. 2, 2015, pp. 5–50.
doi:10.1017/jfm.2015.70

[19] Munters, W., Meneveau, C., and Meyers, J., "Turbulent Inflow Precursor Method with Time-Varying Directions for Large-Eddy Simulations and Applications to Wind Farms," *Boundary-Layer Meteorology*, Vol. 159, No. 2, 2016, pp. 305–328.
doi:10.1007/s10546-016-0127-z

[20] Rapp, S., and Schmehl, R., "Vertical Takeoff and Landing of Flexible Wing Kite Power Systems," *Journal of Guidance, Control, and Dynamics*, Vol. 41, No. 11, 2018, pp. 2386–2400.
doi:10.2514/1.G003535

[21] Zgraggen, A. U., Fagiano, L., and Morari, M., "Automatic Retraction and Full-Cycle Operation for a Class of Airborne Wind Energy Generators," *IEEE Transactions on Control Systems Technology*, Vol. 24, No. 2, 2016, pp. 594–608.
doi:10.1109/TCST.2015.2452230

[22] Fechner, U., and Schmehl, R., "Flight Path Control of Kite Power Systems in a Turbulent Wind Environment," *Proceedings of the 2016 American Control Conference (ACC)*, IEEE Publ., Piscataway, NJ, 2016, pp. 4083–4088.
doi:10.1109/ACC.2016.7525563

[23] Erhard, M., and Strauch, H., "Theory and Experimental Validation of a Simple Comprehensible Model of Tethered Kite Dynamics Used for Controller Design," *Airborne Wind Energy*, edited by U. Ahrens, M. Diehl, and R. Schmehl, Springer, Berlin, 2013, pp. 141–165, Chap. 8.
doi:10.1007/978-3-642-39965-7_8

[24] Booth, J., *A Treatise on Some New Geometrical Methods: The Geometrical Properties of Elliptic Integrals, Rotatory Motion, the Higher Geometry, and Conics Derived from the Cone, with an Appendix to the First Volume*, A Treatise on Some New Geometrical Methods, Longmans, Green, Reader, and Dyer, London, 1873.

[25] Holzapfel, F., and Sachs, G., "Dynamic Inversion Based Control Concept with Application to an Unmanned Aerial Vehicle," *AIAA Guidance, Navigation, and Control Conference and Exhibit*, AIAA Paper 2004-4907, 2004.
doi:10.2514/6.2004-4907

[26] Åström, K. J., and Hägglund, T., *Advanced PID Control*, ISA—The Instrumentation, Systems and Automation Soc., Research Triangle Park, NC, 2006.

[27] Karlsson, E., Schatz, S. P., Baier, T., Dörhöfer, C., Gabrys, A., Hochstrasser, M., Krause, C., Lauffs, P. J., Mumm, N. C., and Nürnberger, K., et al., "Automatic Flight Path Control of an Experimental DA42 General Aviation Aircraft," *2016 14th International Conference on Control, Automation, Robotics and Vision (ICARCV)*, IEEE Publ., Piscataway, NJ, 2016, pp. 1–6.
doi:10.1109/ICARCV.2016.7838566

[28] Bacon, B. J., Ostroff, A. J., and Joshi, S. M., "Reconfigurable NDI Controller Using Inertial Sensor Failure Detection amp;amp; Isolation," *IEEE Transactions on Aerospace and Electronic Systems*, Vol. 37, No. 4, 2001, pp. 1373–1383.
doi:10.1109/7.976972

[29] Lu, P., van Kampen, E.-J., de Visser, C., and Chu, Q., "Aircraft Fault-Tolerant Trajectory Control Using Incremental Nonlinear Dynamic Inversion," *Control Engineering Practice*, Vol. 57, Dec. 2016, pp. 126–141.
doi:10.1016/j.conengprac.2016.09.010

[30] Schreuder, E. N. J., "Improving Winch Control Performance in Kite Power Systems Using Gain Scheduling and a Compliant Element," Master of Science Thesis, Delft University of Technology, Munich, 2013, http://resolver.tudelft.nl/uuid:265aa8d7-7ccf-4257-a22b-ff94b8fe4556.

[31] Föllinger, O., *Regelungstechnik*, 12th ed., VDE Verlag GmbH, Berlin, 2016.

[32] Lavretsky, E., and Wise, K. A., *Robust and Adaptive Control*, Springer–Verlag, London, 2013.
doi:10.1007/978-1-4471-4396-3

[33] "IEC 61400-1 Wind Turbines—Part 1: Design Requirements," International Electrotechnical Commission Tech. Rept. EC 61400-1:2005, Geneva, 2005.